TEMPERATURE, SIZE, AND ENERGY OF THE SHOEMAKER-LEVY 9 G-IMPACT FIREBALL

R. W. Carl son*, P. Drossart†, Th. Encrenaz†,

P.R. Weissman*, J. Hui*, and M. Segura*

* Jet Propulsion Laboratory
California Institute of Technology
Pasadena, California 91109

† Department de Recherche Spatiale
Observatoire de Paris-Meudon
92195 Meudon Cedex

Submitted to Icarus: May 1996
Revised: April 1997

Pages of text: 65 + Title
Number of Tables: 1
Number of Figures: 11
Keywords: Comets, Impact Processes,
Infrared Observations,
Jupiter, Spectrophotometry

e-mail: rcarlson@jpluvs.jpl.nasa.gov
Tel No: (818) 354-2648
Fax No: (818) 393-4605

Suggested Running Title:

SHOEMAKER-LEVY 9 G-IMPACT FIREBALL

Address for correspondence:

R. W. Carlson
Mail Stop 183-601
Jet Propulsion Laboratory
California Institute of Technology
4800 Oak Grove Drive
Pasadena, CA 91109

ABSTRACT

The fortunate position of the *Galileo* spacecraft provided us with a unique opportunity to directly observe the Shoemaker-Levy 9 impacts as they occurred on the far side of Jupiter, and we present observations of the G fireball obtained by the Near Infrared Mapping Spectrometer (NIMS). These measurements were performed using ten spectral bands, four representing continua and spanning the wavelength range 1.84 to 4.38 pm. Fireball signals were evident for up to 80 seconds, with the time of intensity maxima and duration being greater for longer wavelengths. Color temperatures and effective emitting areas were estimated by fitting blackbody functions at the four continuum wavelengths. Good blackbody fits were found, and their intensities at shorter wavelengths shows excellent agreement with the *Galileo* Photopolarimeter/ Radiometer measurements. Temperatures near the beginning are above 3000 K, decreasing to -1000 K after one minute. The corresponding areas range from 400 km^2 to 20,000 km^2. The effective diameter of the luminous fireball shows approximately linear time variation, at least for the first 45 sec. From the temperature-effective diameter relation we find an adiabatic coefficient of y = 1.2 ± O. 1, much as expected from theoretical considerations. The luminosity, when integrated over the period of observations and assuming a Stephan-Boltzmann radiator, gives an above-cloud radiative energy loss of 0.48 ± 0.13 x 1025 erg.

As a conceptual aid, we developed a simple, heuristic theory of the fireball phenomena, considering the penetrating fragment's wake (termed debris channel) to consist of high temperature Jovian and cometary material, which undergoes radial expansion and acceleration back along the wake axis. The outer layer of the material in this debris channel is presumed optically thick, radiating as a blackbody to produce the observed emissions (we speculate that the opacity is produced by condensed refractories such as MgO and SiO_2, probably containing impurities). One-dimensional, variable-area axial flow of a radiating, compressible, inviscid gas

is concurrently solved with the radial shock motion occurring in the non-axisymmetric atmosphere. We calculate debris surface radii and velocities using Sedov's theory for line explosions. The assumed initial debris surface temperature is consistent with entry shock heating. Our simple model shows good agreement with the observations, both for the temperature and luminous area, and suggests that the diameter of the G fragment (assumed spherical and of unit density) was 300 ± 100 m, with a nominal energy of 2.5 x 1026 erg. The measured luminous energy is within a factor of two of that predicted for the nominal impactor size, while the amount of water in the splashback, as measured by Bjoraker et al. and Encrenaz et al., agrees to a factor of three with the model results. However, the large CO abundance obtained by Lellouch et al. is inconsistent with the suggested size. This diameter estimate must be considered provisional and probably a lower limit; precise estimates require comparison of the measurements with comprehensive numerical simulations, which we encourage.

I. INTRODUCTION

The *Galileo* spacecraft's direct view of the Shoemaker-Levy 9 impact events on Jupiter in July 1994 permitted us to study the fireball and subsequent splash phases, the former phenomenon being unobservable from Earth. In this hot, energetic, and explosive first stage, cometary and Jovian material is propelled upward, eventually forming the high altitude plumes, which then fall back onto the atmosphere and produce the splash phase observed from the ground as the "main event". Characterizing this initial fireball period is essential for understanding the entire impact process and the physics of large atmospheric impacts. A summary of current knowledge of the Shoemaker-Levy 9 collision events is presented in the recently published book edited by Nell et al. (1996).

The Near Infrared Mapping Spectrometer experiment (NIMS) onboard *Galileo* observed several of these events (C, F,G,R) and the stored data for the G and R impacts were later telemetered to Earth, along with pre-impact reference observations of the undisturbed Jupiter. Initial reports of these observations have been published (Carlson et al., 1995a, 1995 b), giving preliminary descriptions of the two phases (fireball and splashback) observed by the NIMS instrument. Recent NIMS splash phase results can be found in Encrenaz et al. (1997) and Drossart et al. (1997). Here we concentrate on one aspect of one collision event - the G fireball - and further restrict our discussion to the temperature and size development of this feature and to the energy involved in its formation. Comprehensive analysis of gaseous absorption bands which are present in the fireball spectrum will be presented later.

Because of the rapid development of the fireball and the intermittence of the required NIMS scan pattern (see below), a complete spectrum could not be obtained. Instead, observations were made in seventeen fixed wavelengths, corresponding to a fixed position of the diffraction

grating and the seventeen individual detectors in the spectrometer focal plane (see Carlson et al., [1992] for a description of the NIMS instrument). The chosen grating position gave a set of wavelengths that included four widely separated continuum channels: 1.84, 2.69, 2.97, and 4.38 μm (see next Section and Table 1). These four continuum wavelengths were used to determine temperatures and emitting areas, derived from the spectral shape and the absolute flux levels respectively.

Temporal development of the G fireball is illustrated in Fig. 1, which shows the light curve for each of these continuum channels. The relative time t = O corresponds to the initial observation of the G impact luminosity recorded by the *Galileo* Photopolarimeter/ Radiometer (PPR, Martin et al., 1995) and Ultraviolet Spectrometer (UVS, I-lord et al., 1995) experiments whose results are also shown in the figure. The ultraviolet (0.292 μm) flash occurred the onset and any duration was less than 11 see, while the PPR signal (0.945 μm) was detected for approximately 30 sec. The fireball event, as viewed at our infrared wavelengths, is seen over a period of about one minute, with longer durations observed at the longer wavelengths. During that period, some of the hot gas produced in the airburst is accelerated back along the low density entry wake, and expands in radius to form the observed fireball. Isentropic expansion cools the fireball, shifting the spectrum to longer wavelengths (see Fig. 1) until it is too cold to be discerned by the NIMS instrument. Theoretical predictions and numerical simulations of the fireball development have been given by Ahrens et al. (1 994), Boslough et al. (1994, 1995), Chevalier and Sarazin (1994), Crawford et al. (1994, 1995), Crawford (1996), Shoemaker et al. (1 995), Takata et al. (1994), and Zahnle and Mac Low (1994).

We assume that the fireball can be described as a blackbody radiator, at least for the chosen wavelengths, and that the emissions observed at the four continuum wavelengths originate from a common layer, presumably an optically thick surface at *or* behind the debris front. The

spectra appear to support the blackbody assumption over a surprisingly large temperature range. The opacity sources that may be operating are discussed at the end of this paper.

The temperatures and emitting areas (or equivalently the effective diameter of a quasi-spherical fireball) derived in this work will be used to find expansion rates and to study the thermodynamic properties of this phenomenon. It also seems plausible that the evolution of the fireball temperature and size is related to the energy released in the impact - the kinetic energy of the incoming fragment. This is best studied with numerical simulations, of the type referenced above. However, there is presently no comprehensive set of simulations which couple three-dimensional kinetics with opacity sources and radiation, so an accurate determination may not be attainable at present, although progress is rapidly being made (D. Crawford, private communication, 1996) and such simulations may be possible in the near future. In the meantime, we present here a heuristic theory of fireball evolution, hoping to elucidate the relevant physics and to obtain a first order energy estimate.

With this brief introduction, we next describe the NIMS observations, giving the wavelengths used, the scan geometry, and characteristics of the instrument for point sources (Section 11, following). Analyses of the data, including background subtraction and corrections for cloud reflection are given in Section III. The resulting temperatures, areas, effective diameters and other derived results are then presented (Section IV). Following this, a simple, heuristic model of fireball evolution and emission properties is presented (Section V). The model and observations are then compared, deriving a first order energy estimate. Opacity sources are also discussed in this Section (VI). A summary follows (Section VII).

11. OBSERVATIONAL DETAILS

Observed Spectral Bands

The NIMS instrument was operated in the Fixed Map mode (Carlson et al., 1992), in which the observed wavelengths are arranged in a comb-like pattern of seventeen simultaneously measured spectral positions. The position of the comb is selectable. Prior to the events, we chose a setting which provided measurements at an H_3^+ wavelength as well as at 2.7 μm, a Jovian continuum region between methane and ammonia absorption features (see Carlson et al., 1996; Drossart and Encrenaz, 1983; and references therein). With this choice, the remaining wavelengths are determined and included both continua - where Jovian gas is transparent - and regions of varying gaseous absorption, mainly by methane and molecular hydrogen. The complete set of observing wavelengths is given in Table 1.

At the short-wavelength end of the spectrum (0.71 - 1.56 pm), the solar spectrum is intense and the Jovian albedo is high. The Jovian reflected sunlight spectrum is therefore much greater than the fireball signal, rendering these channels unusable for analysis. At the long-wavelength end, Jovian thermal emission is likewise more intense than the fireball, and the same limitations occur. Ten spectral channels, covering the 1.84 - 4.38 μm region, remain to give useful spectral data.

Continuum wavelengths, i.e. those unaffected by gaseous absorption, depend upon the level in the atmosphere. In previous work (Carlson et al., 1995a) it was found, based upon the depths of methane and molecular hydrogen absorption features, that the *effective* radiating surface of the fireball was in the lower stratosphere or upper troposphere. At these levels, ammonia and phosphine are greatly depleted and do not contribute significantly to absorption, nor do the

weaker methane bands (Husson et al., 1986; Strong et al., 1993). The wavelengths 1.84, 2.69, 2.97, and 4.38 μm (detectors 6, 9, 10, and 15) are found to be sufficiently transparent at these altitudes so they can be used for blackbody temperature and size estimation (see Fig. 3). It should be noted that the GEISA data base (Husson et al, 1986) and Strong et al.'s (1993) measurements differ for the 1.84 μm channel, the former listing no absorption lines whereas the latter shows that the effective absorption would be about 5% for the initial spectrum of Fig. 3a, with less absorption occurring thereafter. This absorption is sufficiently small that it is neglected here. We also emphasize that the concept of a single effective absorption level is quite artificial; proper evaluation must include the vertical profile of the fireball luminosity.

The geometric albedo of Jupiter is also shown in Table 1, and will be used to correct for the cloud-reflected component of the fireball signal. The albedo values were derived from pre-impact reference spectra of Jupiter obtained by NIMS four days before the G event and during the minutes just prior to the G and R impacts. The data were obtained with the same instrumental settings and the same scan pattern. The spectra were averaged and relative albedos generated by dividing by a solar spectrum. They were then normalized (in the least squares sense) to Karkoschka's (1994) geometric albedo values at 0.71 and 0.85 pm, convolved with the NIMS slit function. The ratio of NIMS-derived albedos for the two wavelengths agrees with the corresponding ratio from Karkoschka's data to within 5%, the difference possibly due to the different phase angle. At 2.69 pm, our geometric albedo $(a_g = 0.21)$ agrees quite well with the planar Lambertian albedo ($a_L = 0.3$) derived by Drossart and Encrenaz (1983) when one recalls that $a_g = (2 / 3)\, a_L$ for a Lambertian sphere.

Geometry and Scan Motion

At the time of the G impact, which occurred on 18 July 1994, *Galileo* was at a distance 1 = 239.82 x 106 km from Jupiter. NIMS' effective field-of-view is 0.5 mrad x 0.5 mrad, so the equatorial diameter of Jupiter subtended 1.19 pixels. At the phase angle of 51.3 deg, a large

portion of the disc was sunlit. This, and the comparable angular sizes of Jupiter and a NIMS pixel, caused most of our fireball measurements to include reflected sunlight from the dayside, and this amount varied from one observation to the next. The zenith angle of the spacecraft - the emission angle - at the time and location of the G impact was 67.33 deg, giving an airmass factor of 2.59. The geometry is shown in Fig. 2.

Owing to pointing uncertainties, it was necessary to scan a large area around the predicted location of Jupiter. This was accomplished with one-dimensional spatial scanning produced by the NIMS instrument coupled with orthogonal spacecraft scan-platform motion (see Fig. 2). NIMS scanning produces a linear column of twenty pixels oriented in the "cross-cone" or azimuthal direction (relative to the spacecraft axis). The spacecraft scanned in polar angle or the "cone" direction. One-way travel time for the cone angle scan was 5 1/3 see, which establishes our temporal resolution. The cone angle scan rate was 0.92 mrad see^{-1}. Since it takes 1/3 sec to generate the twenty-pixel column, adjacent columns of pixels (at the center of the column) are separated by 0.31 mrad. For a field width of 0.5 mrad, there is approximately 40?4. overlap so in general one, and often two, mirror-scan columns will contain fireball signals. Within a column, usually two pixels were illuminated by fireball emissions due to overlap in the cross-cone spatial response (see below).

Point Source Instrument Response

The fireball it is effectively a point source, and response variations over the instantaneous field of view must be considered when deriving spectra and absolute intensities. We first discuss the shape of the spatial response function and show that it is possible to obtain accurate measurements which are independent of position, at least to first order. Instrument calibrations appropriate for point sources are then described.

In the cone direction (see Fig. 2 and caption), the response is rectangular, while in the cross-cone direction astigmatism in the spectrometer broadens the spatial response and produces a sensitivity profile which is approximately triangular in shape. The width of this triangular response produces overlap between successive pixels in a column, so signals from a point source usually appear in two adjacent mirror scan pixels. Since the spacing and width of the overlapping pixels are nearly identical, the sum of the signals for the two affected pixels is nearly independent of the relative location within the pixels (e. g., for a point source at the center of a pixel, the full signal will appear in one mirror position; if midway between two pixels, then two mirror positions will show signals, each at half intensity; etc.).

We have performed in-flight investigations of the accuracy of this two-pixel-sum method, determining inter-spectrum fluctuations that can arise from non-ideal response and pointing differences (jitter). Using observations of α-Ori, deviations from the average using two-pixel sums were found to be approximately ± 1 %. Such deviations probably account for much of the noise evident in light curves of Fig. 1.

In addition to the spectrum-to-spectrum jitter noise discussed above, one must also consider intra-spectrum noise, that is: does the jitter discussed above affect all wavelengths equally? The α-Ori data were examined for this effect, comparing the signals at one wavelength relative to another within the same 17-channel spectrum. These data show that the modulation between measured and nominal values, within a given spectrum, is less than 5% (at the one standard deviation level).

The instrumental calibration for point sources, obtained from laboratory measurements, can be compared to in-flight observations of standard stars. Using NIMS observations of α-CMa and the airborne measurements by Strecker et al. (1979), a set of in-flight NIMS calibration values

were derived and compared to the laboratory values. The ratios of the stellar and ground calibration values were found to be constant over wavelength to within eight percent, a limit imposed largely by noise in the relatively low infrared flux levels measured from Sirius. The mean ratio of the two sets is 0.87. It is unclear whether this difference from unity is due to systematic errors in the NIMS laboratory measurements and/or the airborne flux data, or simply due to spatial response variations in NIMS, discussed above. We assume the latter, more likely case, and assert that the good spectral agreement between the laboratory and flight calibrations justifies *use* of the laboratory values in this analysis.

Noise Levels

We are concerned here about noise levels within an individual spectrum which influence the derived temperature values. Two sources contribute to the noise level of the measurements: the intrinsic noise level of the instrument and the fluctuations due to the wavelength-to-wavelength jitter. The spectrum-to-spectrum jitter discussed above only produces a variance in the overall level and thus the derived emitting area.

The noise level of the instrument, in the gain state used for the Shoemaker-Levy 9 measurements (Gain State 2), is 0.7 to 1.0 data numbers (DN) while typical signals were 10 to 20 DN. (Knowledge of dark level is within 0.03 DN so it is an insignificant source of systematic error). The intra-spectrum wavelength-to-wavelength noise, discussed above, is 5 % of the total signal, fireball plus reflected sunlight. Using these values, the root-mean-squared deviation in the source intensity is u ≈ 29 TW $ster^{-1}\,\mu m^{-1}$ (the average squared-deviation was obtained using all of the spectra in the fireball period). Since the average source intensity is about 200 TW $ster^{-1}\,\mu m^{-1}$, then the fractional error is of order 15%.

111. DATA REDUCTION AND ANALYSIS

The summed data numbers, after dark subtraction, consist of two components - the fireball signal and background radiation from Jupiter, the latter arising from reflected sunlight and thermal emission occurring in the 5 μm region. The fireball signal itself contains two components, radiation received directly from the fireball and light reflected from the underlying clouds.

Our general analysis procedure is to subtract the Jovian reflected solar component, apply the instrumental calibration, correct for the cloud reflectivity, and then fit the shape of the resulting spectra with a blackbody function to obtain the temperature. From the temperature and absolute source intensity, the subtended emitting area is derived. Since the fraction of the original signal which is due to reflected sunlight is not precisely known and is different for each spectrum, we consider this a free parameter (within limits) and use an iterative procedure to find the best fitting temperature, area, and solar contribution. Details of the procedure are discussed below.

Background Subtraction

In this work, we employ two average Jupiter reference spectra for background subtraction. Both spectra were obtained from NIMS observations, using the same conditions as the impact observations. The first spectrum (Case 1) used the Jupiter reference observations, obtained on 14 July 1994, as well as observations of Jupiter during the minutes just before the G and R collisions. The entire disc of Jupiter was included in generating this average spectrum. The advantage of this case is the large number of spectra used to find the average. Its disadvantage

is that it includes the midmorning-to-midafternoon hemisphere as well as the night-to-dawn hemisphere where the impact events occurred, and was obtained for three different sub-spacecraft longitudes. Case 1 was used to generate the geometric albedos of Table 1. In the second case (2), we used just those spectra obtained during the ninety second period before the G impact and further restricted the spectra to those for the night-dawn hemisphere only. The average spectrum obtained for this case obviously relates better to the G event, but the number of spectra comprising this average is small and its statistical quality may be poorer.

In our earlier work (Carlson et al., 1995a,b) we assumed that the signals occurring in our shortest wavelength detector (Det. 1, 0.711 μm) were largely due to the intense reflected sunlight component found at short wavelengths with little contribution from the fireball itself. The average reference spectrum (Case 1) was then normalized to the Detector 1 value and the entire normalized spectrum subt ratted from the observed spectrum. Preliminary temperatures and areas were obtained using this procedure. Although this method provides a good first approximation, it can be improved as follows. As before, we generate normalized spectra, but refine our procedure and subtract a fraction η (discussed below) of the normalized spectra. The fraction η is varied, iterating to find the best fit.

Jovian thermal emission is very bright in the 5 μm region, and this component in our spectra overwhelms the fireball signal for Detectors 16 and 17 (4.67 and 4.95 pm). We have not attempted to perform any correction to extract impact-related signals for these wavelengths. We have, however, checked for any thermal emission contribution to the 4.38 μm channel (Det. 15) by performing a regression analysis with the higher wavelength channels. Little correlation was found, and we can place an upper limit on thermal contributions to the signal of 3 TW $ster^{-1}$ μm^{-1}. Referring to Fig. 1d, this is a small contribution, if present at all. Even if it is present, it will be partially corrected for in the subtraction of the normalized reference spectra.

Source Intensities

It is convenient to express our results in quantities which are independent of the instrument and its distance to the source. As the fireball is quite small compared to the projected pixel size, photometric quantities related to point sources are appropriate. The spectral luminosity L, the total power radiated per unit wavelength interval, comes to mind immediately but this is inappropriate since we do not have experimental knowledge of the angular radiative properties. A more directly measured parameter is the power radiated per unit solid angle in the direction of the observer, termed the radiant source intensity S or the pointance (see Wyatt, 1978, p. 46 ff.). To arrive at this quantity, referred to simply as the source intensity, we use the laboratory-derived sensitivities, which give data numbers (DN) per unit radiance. For point sources, the so-derived, fictitious radiance is the mean brightness for the pixel area projected at Jupiter, so multiplying the radiance by this area gives the source intensity. For an isotropic radiator, this source intensity is related to the luminosity as $L = 4\pi S$.

Cloud Reflection Correction

Fireball radiation reflected by the underlying clouds will contribute to the observed signals, and will do so in a wavelength dependent fashion. We can correct for this added component, using an approximate correction factor derived below.

Consider a source at altitude z above the clouds, with source intensity S. At a radial distance R from the nadir point, the irradiance, normal to the direction of propagation, is $\pi F = S / (z^2 + R^2)$. The power incident on the cloud per unit area is $\pi F \mu_0$ with μ_0 being the

cosine of the zenith angle ($\mu_0 = z/\sqrt{z^2 + R^2}$). When diffusely reflected with Lambertian albedo a_L the surface brightness (radiance) is $I = \pi F \mu_0 (a_L/\pi)$. The additional power radiated per unit solid angle at the emission angle $\cos^{-1}(\mu)$ is the integral of radiance over the projected area:

$$S = 2\pi\mu \int_0^x I R\, dR \qquad (1)$$

Integrating, we find

$$S + AS = (1 + 2a_L\mu)S = (1 + 3a_g\mu)S \qquad (2)$$

where we used the well known relation $a_g = (2/3)a_L$. Thus, the reflectivity correction factor is $1/(1 + 3a_g\mu)$. The correction for cloud reflectivity is generally small (correction factors near unity) since Jupiter is dark at most of the wavelengths employed here, except for the 2.69 μm signals where the correction factor is -0.81. Even for that wavelength, errors in the albedo determination or non-Lambertian behavior of the reflecting layer do not lead to significant errors in the source intensity; a 30% error in a_g leads to a 6% error in the 2.69 μm correction factor.

Temperature and Area Determination

The temperatures and emitting area determinations are found using the following procedure. For a given spectrum of summed and dark-corrected pixel-pairs, we normalize the Jupiter reference spectrum to the 0.711 μm signal. A fraction η of this normalized reference spectrum is subtracted from the observed spectrum. Corrections for cloud reflectivity and the instrumental calibration are then applied, giving source intensities. We then compute, for a range of temperatures, the emitting areas *A* that give the best least-squares fit of a blackbody

source with the observed source intensities. The fitting procedure minimizes χ^2 for uniformly weighted points, using the mean squared deviation given in Section II (Noise Levels). The resulting χ^2 depends upon the assumed temperature. After finding the temperature that produces the minimum χ^2 (for the assumed η) we then choose another value of η and repeat the procedure. The computation is performed interactively, converging on the set of η, T, *A* that give the lowest χ^2. Error limits (1 -u) in temperature and area are then estimated by finding the T, *A* pairs that give $\Delta\chi^2 \approx 1$ (Bevington, 1969, p. 243).

How robust is this procedure and the corresponding temperature and area determination? After all, given enough parametric functions, one can fit anything. The situation is aggravated if the fitting functions employed are similar in shape, or if the subtracted component is nearly equal in magnitude to the data points to be fitted. Furthermore, inaccuracies in the fitting functions (i.e. errors in the Jovian reflectance spectrum or non-blackbody emission) will influence the validity of the results. These points are discussed below.

In these estimates, we use four data values to determine three parameters - the magnitude of reflected sunlight, the fireball temperature *T* and its area *A* - giving a statistical degree of freedom of unity. The fitted functions are quite dissimilar. In particular, the reflected sunlight contribution is proportional to the solar flux modified by the strongly varying Jovian reflectance (see Table 1), and this contribution is markedly different from the assumed blackbody emission curves, even when the latter includes the relatively minor cloud reflection correction. The relative shapes of these two functions differ over wavelength by more than an order of magnitude, providing easy numerical discrimination between the two. Furthermore, the magnitude of the subtracted reflected sunlight component is generally modest, so the remaining fireball component can be accurately derived. The mean ratio of the fireball signal to the total signal (fireball plus reflected sunlight) for Detectors 6, 9, 10, and 15 is 0.43, 0.41, 0.84, and 0.88 respectively, generally giving fireball contributions well above the noise level. We

also find, as expected if our procedure is correct, that the reflected light contribution (determined by the fitting procedure) is correlated with the strength of the reflected component (measured independently at shorter wavelengths).

We have used the two reference spectra cases discussed above (Case 1, mean full-disc spectrum and Case 2, pre-G impact dawn hemisphere spectrum; see Background Subtraction) and find nearly identical results; the mean temperature difference is - 6 K, and the root-mean-squared deviation is - 25 K. As a further check on the veracity of the method, we used two other methods to determine η. The first employed average correlation parameters for η found in the minimization fits, while the second method simply assuming $\eta = 1$, a rather extreme first-order approximation. In all of these tests, the derived temperatures were within 1.5a and generally much better. The totality of these tests indicate that the reflected component is being treated properly, and that the final results are rather insensitive to the analysis details.

In addition, we note that the distribution of χ^2 values is consistent with that expected for random errors and a degree of freedom of one. This offers statistical evidence that the reference spectra are accurate and that the blackbody assumption for the fireball is appropriate. A more telling test is examination of the spectra themselves and the corresponding fits, presented in the next Section.

IV. RESULTS

We illustrate the quality of the spectral fits by showing two representative spectra (Fig. 3), representing the beginning and middle of the G fireball phase. These particular times were chosen because the light curve data shows maximum response and these data are presumed to be directly comparable to the corresponding PPR values (Martin et al., 1995), which are also indicated in the Figures. (The spectrum-to-spectrum pointing jitter discussed above, which affects the NIMS and PPR measurements differently, generally precludes a direct, quantitative comparison between these two sets of measurements. It is anticipated that they are best related at the higher NIMS signal levels where the pointing is more centered, although one must also be wary of potential calibration differences). The PPR values have been here corrected for cloud reflection using Karkoschka's geometric albedos, averaged over the PPR bandpass. The blackbody curves were generated using the temperature and area parameters derived by minimizing X^2, using the mean full-disc Jupiter reflectance spectrum (Case 1, see Section III Background Subtraction). These parameters are nearly identical to those found using the pre-G impact dawn hemisphere values (Case 2). Absorption by methane has also been included in the figure, and absorption by molecular hydrogen at 2.125 μm is apparent. The methane abundances correspond to stratospheric or upper tropospheric levels for absorption. These spectra, and their level of formation, corroborates our assumption that the four wavelengths used to derive temperatures and areas can indeed be considered continuum wavelengths.

The good agreement between our blackbody fits and the PPR results is quite satisfying. It is additionally important because it indicates that the opacity source producing this thermal emission appears to be quasi-continuous, at least over the interval 0.945 μm to 4.38 μm. We speculate on the opacity source later.

Temperatures, Areas, and Effective Diameters

The time variation of the fireball temperatures is shown in Fig. 4a. Corresponding areas were also obtained, and we have chosen to portray these quantities as effective diameters (Fig. 4b) of the equivalent sphere (or more precisely, of the equivalent circular radiating area), since it is easier to think of linear dimensions. It is important to bear in mind that the fireball is never truly spherical; it probably starts as a cigar-shaped entity and evolves into an egg shape.

It is also important to note that these temperatures and sizes are effective values, and that the temperature distribution of the emitting surface is probably not isothermal. The derived temperatures are, in essence, color temperatures derived from weighted mean intensities. The relationship to true temperatures is unknown, but it is expected that trends in temperature behavior are indicative of physical conditions.

The time reference t = O employed here is that of Fig. 1: the first instance of G impact emissions detected by the Photopolarimeter/Radiometer experiment (see caption, Fig. 1). Using the UVS (Herd et al, 1995) and PPR (Martin et al., 1995) fluxes at t = O and correcting for cloud reflection, we obtain $T(0)$ = 8000 ± 1000 K which seems consistent with the later NIMS measurements (see Fig. 4a). At the time of the first NIMS measurement of fireball emission, (t = 5.17 see) the temperature is approximately 3300 K, which is above the boiling point of most materials, save for some refractory compounds. It is lower than most stellar temperatures, but comparable to the photospheric temperatures of the cool M stars. As time progresses, the temperature continues to decrease, achieving – 1000 K at one minute into the event. Beyond this time, the signal is too weak to enable a temperature measurement.

The effective radiating area *A, also* expressed as an equivalent or effective diameter D_{eff}, is given in Fig. 4b. From these results, one can describe the early size development ($t < 40$ see) as an object whose dimensions expand linearly with time; in particular, the effective diameter expands at about $dD_{eff}/dt = 3.2$ km sec $^{-1}$, which we term the expansion velocity. It is unclear from these data whether the linear expansion continues later in the period, the data perhaps suggesting a constant or decreasing effective area beyond 45 seconds. If so, this behavior perhaps could arise from the fireball becoming optically thin at this time, or from other effects; we will return to this point in Section VI. If the fireball was a point explosion, which it surely was not, then the time origin of the explosion would have been $t_0 = -2$ sec. Assuming adiabatic expansion (see below) and further that the volume V is proportional to $(t - t_0)^3$ (i.e. the dimensions of the fireball vary linearly with time, as suggested by the constant expansion velocity) then the temperature variation can be described as $T = (t - t_0)^{-3(\gamma-1)}$. We have performed a subjective fit of this functional dependence to the derived temperature values, using the approximate adiabatic index γ derived below, producing the curve shown in Fig. 4a. It can be seen to fit the data well and illustrates consistency between the NIMS and UVS/PPR-derived temperatures.

At this point, it is possible to derive a zeroth-order, order-of-magnitude estimate of the fireball energy. Let us assume that the absorption features in the spectrum obtained at 26.5 seconds (see Fig. 3b) are due to absorption by atmospheric gas that the shock wave has passed through and accelerated, so this gas is now entrained in the expanding shock region. If the temperature of this gas is low enough such that the absorption properties resemble that of the unshocked atmosphere, then the surface mass density is - 20 g cm^{-2}, using the C/H ratio of Gautier et al. (1982). For a sphere of diameter 80 km, expanding radially at half the (diametric) expansion rate, the kinetic energy is $E \approx 5 \times 10^{25}$ erg. This estimate does not include thermal or radiated energy, nor the kinetic energy of material in the debris channel, inclusion of which would raise the total energy estimate. It also assumes that all of the absorbing gas is in the

shock region, with no absorption by the exterior atmosphere; allowance for this would lower the estimate. Note that this is a different assumption than used in our preliminary report (Carlson et al., 1995a), where it was assumed that the absorption features arose from atmospheric gas outside the shock boundary, at least during the early fireball period. Reality lies somewhere between these two assumptions. A somewhat better energy estimate is provided in Section VI.

Expansion and the Adiabatic Index

As suggested above, the temperature profile seems to follow an adiabat, and here we explore this thermodynamic behavior in more detail. If there is little heat exchange between the fireball and the surrounding atmosphere and if radiative losses are small, then the expansion process can be considered adiabatic and isentropic. The temperature drops as thermal energy is transformed to expansion and kinetic energy. Recall that the temperature-volume relation for an ideal gas with constant adiabatic index is $TV^{(\gamma-1)} = constant$. The adiabatic index, the ratio of specific heats at constant pressure and volume ($\gamma = c_p/c_V = (c_V + \Re)/c_V$, $\Re$ being the gas constant) is in general somewhat temperature dependent and our observations can be used to determine an average value for γ.

We first estimate the expected value of γ by considering the fireball to include mainly Jovian molecular hydrogen and helium. The atomic specific heat ($c_V = (\partial e/\partial T)_V = (3/2)91$, e being the thermal energy per unit mass) is small compared to that of molecules at high temperature, for which molecular dissociation provides an energy reservoir that increases rapidly as the temperature and dissociation fraction α increases. Using the approximate formulation of Landau and Lifshitz (1980, pp. 308-310), the variation of γ with temperature was found for a Jovian mixture of Hz and He and is portrayed in Fig. 5, along with the dissociation fraction α. An effective value of α = 1.06 - 1.30 is predicted for the assumed gas composition. The

ionization contribution to the specific heat was not included; doing so would increase the specific heat at high temperature, decreasing γ. Adding cometary molecules to the mixture would also tend to decrease y.

The effective adiabatic index for the fireball can be estimated from the NIMS observations by two methods. In the first method, we attempt to estimate γ using temperature and size information directly. We assume that these measurements refer to the same material in the fireball, which act as luminous tracers of the emitting surface, which is expanding and cooling. We also assume, even though the emitting area is likely not isothermal, that our derived effective temperatures and sizes are proportional to adiabatic conditions, and further that the volume V varies as $V \propto A^{3/2} \propto D_{eff}^3$. We will find later (Section VI, Fireball Energy Budget) that the relative radiative energy loss for t >10 sec is less than 10°A of the total. Thus, most of our data represents quasi-adiabaticity.

The observed temperature-diameter relationship is shown in Fig. 6, where an adiabatic relationship would appear as a straight line, with slope of m = -3(Y-1). We have illustrated three such cases along with the observations. If our above assumptions are correct, then a value for in the range of γ = 1.1 - 1.3 is found, with a probable value of γ = 1.2 or perhaps slightly higher.

In the second method, we use the times of the maxima in the light curves (Fig. 1) and the corresponding temperatures to estimate -y. For an isothermal sphere of diameter D, the source intensity is

$$S = \frac{\pi}{4} D^2(t) \varepsilon \, El(T(t)) \qquad (3)$$

where $B(t)$ is the Planck function and ϵ the emissivity. The variation in intensity can be calculated as

$$\frac{dS}{S} = 2\frac{dD}{D} - \frac{dx}{1-e^{-x}} \qquad (4)$$

where x = $hc/\lambda kT$. For adiabatic expansion, and with $V \propto D^3$, we have $dD/D = [3(\gamma - 1)]^* dx/x$ For a given wavelength, the intensity will be a maximum for

$$\gamma = 1 + \frac{2}{3}\frac{1-e^{x_0}}{x_0} \qquad (5)$$

with x_0 given by the temperature at that time. Estimating the times of maximum intensity from the light curves (Fig. 1), and obtaining the temperatures at those times (Fig. 4a), we find values ranging from γ = 1.18 to y = 1.25. From this and the preceding estimate, we surmise that our experimentally determined value of y is consistent with expectations. Perhaps a better way of viewing these results is that the correspondence between measured and expected values demonstrates consistency between the temperature and area determinations.

Luminosity and Radiated Energy

It is of interest to know the total energy radiated by the fireball, but this cannot be found directly from our measurements since some fraction of the radiation could be emitted either below the cloud deck and in wavelength regions not covered by the Galileo measurements. We can, however, estimate the above-cloud component that was emitted during the minute or so of *Galileo* observations. Using the expansion velocity discussed previously, which is applied for the entire time between t = O and t = 60 see, the semi-empirical temperature-time relationship (see Fig. 4a), and assuming an isotropic, spherical, Stephan-Boltzmann radiator, then the total energy radiated between t = O and t = 60 sec is approximately O.61 x 1025 erg. On the other

hand, if we assume that the linear expansion only occurs during the first 45 seconds, after which the effective diameter is constant (see Fig. 4b), we obtain 0.45 x 10^{25} erg. If we consider the fireball as a line source rather than being spherical, the luminosity estimate is reduced by the factor $\pi/4$ when viewed normal to the axis. With the uncertainty in diameter during the latter phase, and the uncertainty in the geometric shape of the emitter, we suggest that the integrated luminosity (0-60 see) from above the cloud deck is 0.48 ± O. 13 x 1025 erg. We will compare this measurement to predictions from our heuristic model described in Section VI (Energy Budget).

V. A HEURISTIC FIREBALL MODEL

We now pause in our discussion of the data and pursue a diversion, developing a description of the fireball phenomena which will be employed subsequently for further interpretation of the data (Section VI). This model will be used as a tool to find, for example, the levels from which the observed emissions emanate, the temperature distribution, the size and shape of the fireball, and a first-order estimate of the energy associated with the G impact. Our goal is to formulate a simple theory, but one which is plausible and contains the salient physics, including radiative loss and expansion in the non-axially symmetric atmosphere. Simplicity is achieved by minimizing the number of free parameters of the theory; here we allow just one parameter, the initial size of the impactor. In doing so, we forfeit some degree of flexibility and accuracy, but avoid contrived solutions. More precise estimates will still require comprehensive numerical simulations.

Qualitative Description

As the comet fragment penetrates the atmosphere, it will form a wake, referred to here as the *entry channel* or *debris channel (see* Fig. 7). The material in this region is heated to high temperature and pressure, and will begin expanding immediately. Initial expansion in the radial direction will be supersonic (with respect to the surrounding atmosphere) and the expanding surface of the channel (termed the *debris front*) will drive a cylindrical shock wave. At the same time, the pressure gradient along the channel, caused by the increasing energy deposition as the fragment descends into the denser atmosphere, coupled with radial expansion behind the fragment, will produce an axial force on the channel material in the back direction. Axial acceleration of the wake gas and conversion of thermal to kinetic energy will cause, at any

given point along the axis, the pressure (which drives the shock wave) to vary with time, as energy is transported along the axis. The Reynolds number of the debris gas will be very large, so one expects turbulent motions and associated large eddies, particularly for the core of the debris channel (Landau and Lifshitz, 1959; §§ 31, 36). In this case, the eddy (or turbulent) viscosity will be large, and the debris material at any given axial distance will be coupled, tending to move as a unit along the axis. Turbulence will also act toward reducing temperature and density gradients in the radial direction, but rapid radial expansion can reduce this mixing. Even with non-uniform radial density and temperature distributions, the pressure distribution within the channel is expected to rapidly achieve near-isobaric conditions in the radial direction. Because of the high Reynolds number of the gas, true viscous effects are expected to be important only in a thin layer between the axially moving debris channel gas and the atmospheric gas in the shocked region outside (Landau and Lifshitz, 1959, p. 310). We therefore assume negligible viscous interaction between the two, so the shocked atmospheric gas moves only radially. (Across a shock front, the transverse velocity component is conserved (Landau and Lifshitz, 1959, p. 3 18) so the atmospheric gas in front of the shock, having zero velocity, has no axial velocity component after the radially-directed shock passes through.)

All the while these motions take place, the hot debris gas will radiate energy. There will be some contribution of cometary material to this gas (hence the term debris channel), and this cometary fraction will contain atoms, molecules, condensates, and the easily ionized metals Na, Fe, Ca, Li, K, and Mg (Roos-Serote et al., 1995; Weaver et al, 1995). Such a mixture can form efficient optical opacity sources, e.g. the H continuum and others discussed later, so we make the assumption that the outer surface layer is optically thick at the wavelengths observed. This seems a justifiable assumption, since if the fireball were optically thin then the emission rate would depend only upon the number of emitting particles, and for a roughly constant number of emitters there would be no apparent change in emitting area, even as the fireball expands. The gas in the shock region, composed of Jovian gas, will be generally cooler so it will not be an

efficient radiator, except perhaps in strong molecular bands (e.g. at 3.25 pm, the C-H stretch band, see Fig. 3 and Carlson et al., 1995a).

Our model, whose quantitative formulation is given below, determines the axial velocity using the equations of motion for non-steady quasi-unidimensional hydrodynamic flow with variable area for a compressible, inviscid gas. This motion is coupled to the radial outflow through the instantaneous pressure within the channel and the work performed on the atmosphere to produce the outward flowing shock. Loss of energy of the debris channel gas by radiation is also included. The radial flow will be azimuthally asymmetric because the fragment penetrates the atmosphere at an oblique angle (00 = 45 deg). The corresponding azimuth-dependent force equation includes the back pressure of the atmosphere and therefore approximates both strong and weak shock conditions. The location of the debris front relative to the shock front and the velocity structure behind the shock are determined using Sedov's (1959) theory for line explosions. We assume an initial debris surface temperature consistent with entry shock heating in front of the penetrator (Chevalier and Sarazin, 1994; Zahnle and Mac Low, 1994) and describe the subsequent temperature development as proportional to the evolving thermal energy content. Orton's (1981) model of Jupiter's atmosphere was used, with the Jovian gas assumed to consist of hydrogen and helium only. For the cometary gas, we use the abundances of Anders and Grevesse (1989, Table 7), which is based in part on Jessberger et al.'s (1988) measurements of Comet Halley.

Quantitative Formulation

As noted above, we approximate the fireball development by separately and simultaneously solving for the axial and radial motions, which are coupled through the time-varying energy density within the channel and work performed on the atmosphere. We first describe the axial

flow. It was suggested earlier that turbulence will promote the debris channel material to move locally as a unit along the wake axis (denoted by the variable s, positive upward). We explicitly assume this coherent motion, and define, for the debris channel, the linear mass density $\hat{\rho}(s,t)$ and mean density $\bar{\rho}(s,t)$, related as:

$$\hat{\rho}(s,t) = \int \rho(s,t)dA = \bar{\rho}(s,t)A_d \tag{6}$$

where A_d is the cross-sectional area of the debris channel and $\rho(s,t)$ is the density. In like manner, the quantities p and $\bar{p}$ are formed from the pressure p:

$$\hat{p}(s,t) = \int p(s,t)dA = \bar{p}(s,t)A_d \tag{7}$$

For one-dimensional motion with variable area, the continuity equation for mass conservation, expressed using the substantive or Eulerian derivative $D/Dt = \partial/\partial t + u\,\partial/\partial s$ with u being the axial velocity, is (Stanyukovich 1960, p.48; Ginzburg, 1963, p. 107)

$$\frac{D\hat{\rho}}{Dt} + \hat{\rho}\frac{\partial u}{\partial s} = 0 \tag{8}$$

The momentum equation, for the variable area case, is unchanged from its strictly one-dimensional form, so long as ∂A_d /as is small (Stanyukovich, 1960, p. 48). With our assumption of radially uniform axial motion, and using the quantities defined above, the axial velocity u is described by

$$\hat{\rho}\frac{Du}{Dt} = -A_d\frac{\partial \bar{p}}{\partial s} \tag{9}$$

The energy equation is also unchanged from the constant area case if radial motions are small (Stanyukovich, 1960, p. 48). In the fireball motions encountered here, the mean squared radial velocities $\langle v^2 \rangle$ can be comparable to the axial velocities, so a better approximation is obtained

by including the radial kinetic energy term, resulting in (cf. Liepmann and Roshko, 1956, pp. 186, 190):

$$\hat{\rho}\frac{D}{Dt}\left[h+\frac{1}{2}u^2+\frac{1}{2}\langle v^2\rangle\right]=A_d\frac{\partial p}{\partial t}-\hat{q}_{rad} \qquad (10)$$

Here, h is the average value for the enthalpy (or heat content), defined here as $h=\left[\gamma/(\gamma-1)\right](\hat{p}/\hat{\rho})$. The first term on the right is called the flow work (see Liepman and Roshko, 1956). Energy lost through radiation (per unit axial length) is represented by the $\hat{q}_{rad}$ term and discussed below. Work done on the atmosphere is contained in the time variation of the enthalpy, specifically through a term $\bar{p}\,\partial A_d/\partial t$ denoted here as $\dot{q}_{pdV}$. Knowing the radius $r_d(\varphi,s,t)$ and velocity $v_d(\varphi,s,t)$ of the debris front as a function of the azimuthal angle φ, the work expended on the atmosphere in driving the cylindrical shock is evaluated as

$$\hat{q}_{pdV}(s,t)=\int_0^{2\pi}d\varphi\, r_d(\varphi)\,\bar{p}\,v_d(\varphi) \qquad (11)$$

We approximate the radial kinetic energy of the debris gas by assuming that this mass is concentrated toward the periphery (as suggested later) and moves radially at the debris front velocity $v_d(\varphi)$. We will find that the radial kinetic energy is a small fraction of the total, so errors in this assumption are not significant.

We assume that the debris channel is of sufficient optical thickness that we can regard the debris front as the radiating surface. The radiative loss rate is

$$\hat{q}_{rad}(s,t)=\int_0^{2\pi}d\varphi\, r_d(\varphi)\,\sigma\varepsilon T_d^4$$

where σ is the Stephan-Boltzmann constant, ϵ the emissivity (assumed unity in all of these calculations), and $T_d(s,t)$ the debris front temperature. Because of the strong T_d^4 dependence

and the finite thermal capacity, the temperature variation during each integration time step can be significant, so we find the temperature profile during each iteration period by including the change in thermal energy due to radiated heat:

$$\frac{d}{dt}\left[m_d(\varphi)c_p T_d\right] = -\sigma\varepsilon T_d^4 \tag{13}$$

finding $T_d(s,t)$ and then using that result to obtain $\hat{q}_{rad}(s,$ t). Here, $m_d(\varphi)$ is the debris channel mass distribution per unit azimuthal angle and per unit length.

The exploding debris channel can be thought of as a radially expanding piston, entraining atmospheric gas as it expands. The shocked gas is accelerated, compressed, and heated in a thin layer, the inner surface being at the debris front (the piston) and the outer boundary called the shock front. We denote the radii and velocities of the debris front and shock front as r_d,v_d, r_s, and c_s, respectively. With $m_s(\varphi,s,t)$ representing the mass per unit angle behind the shock front, the momentum change is

$$\frac{d}{dt}\left[m_s(\varphi)v\right] = f \tag{14}$$

where v is an effective velocity (related to c_s) and the force is

$$f = r_d\bar{p} - r_s p_a + \zeta(r_s - r_d)\bar{p} \tag{15}$$

where $p_a(\varphi)$ is the exterior atmospheric pressure at the shock front. The first and second terms for f represent the debris channel and atmospheric pressure forces respectively; the third term is the pressure force of the adjacent gas in the shock region, of average pressure $\zeta\bar{p}$. Taken as a whole, this latter term describes the overall net outward expansion of a cylindrical annulus of pressurized gas, The pressure within this shocked gas is related to the central pressure

through the approximate proportionality factor $\zeta = (3\gamma - 1)/(\gamma + 1)$ derived here using the simple shock wave formulation of Chernyi (Zel'dovich and Raizer, 1966, pp. 97-99). Using Sedov's [1959) theory for cylindrical shocks, we find can solve for v and c_s, and then integrate to find the shock radii $r_s(\varphi)$.

Having obtained the radius and velocity of the shock for various azimuthal angles, the location of the debris front and its velocity can be found, again from the Sedov formulation. Sedov computes the radial position of Lagrangian particles which were initially at the boundary, when the shock was smaller in radius. For the initial debris channel radius r_0, its subsequent radial position r_d can thus be found (Sedov, 1959; p. 219), knowing r_s. Similarly, with the radius r_d determined, the velocity v_d at that point can be computed. We assume that the central position of the channel can move off axis as the outer regions respond to the varying atmospheric density and pressure.

It is impossible to determine the debris front temperatures with any certainty; in the following we can only attempt to formulate a rational and consistent estimate. We first assume that the surface temperature is proportional to the mean energy density, specifically being a factor ξ of the temperature that would be found if debris channel pressure and density were uniform:

$$\Re T_d = \xi\ (p/\rho) = \xi(\hat{p}/\hat{\rho}) \qquad (16)$$

To estimate the initial value of ξ, consider the fragment as it is penetrating into the atmosphere and depositing energy into the interacting atmospheric gas and the ablated cometary material. Just behind the leading surface of the fragment, this gas is presumed to be contained within an annular ring whose radius is r_0 and for which the width is of order the entry shock standoff distance $\delta = r_0(\gamma - 1)/(\gamma + 1)$. The gas contains considerable thermal and kinetic energy, and the high velocity components will implode into the vacuum behind the fragment, disproportionately

carrying energy into the center and producing the isobaric channel. If half of the mass implodes into the *core,* then we find $\xi = 4(Y - 1)/(y + 1) \approx 1/3$. Through a somewhat different line of reasoning, Zahnle and Mac Low (1994) find temperatures equivalent to $\xi \approx 1/4$. Using our assumption above ($\xi = 1/3$), the initial maximum debris surface temperature is approximately 40,000 K, obtained for the impactor traveling at $v_o = 60$ km sec^{-1} which is consistent with the entry shock temperatures obtained by Chevalier and Sarazin (1994, their Fig. 2) and Zahnle and Mac Low (1994, their Fig. 3). The subsequent surface temperature evolution is described, for reasons of simplicity and from ignorance of the behavior of large fireballs, using the same relationship as above; $\Re T_d \approx (1/3)(\hat{p}/\hat{\rho})$. This implies self- similar behavior for the radial temperature and density profile, with lower temperatures and higher densities occurring at the periphery of the debris channel. Turbulence will tend to alter this self-similar structure, and we will find evidence that this assumption is inaccurate during the latter half of the fireball phase.

We now establish the initial conditions - the energy deposited in the entry channel as the fragment descends into the atmosphere. The energy deposited per unit length $\varepsilon(s) = dE/ds$ has been discussed by many authors (Ahrens et al. (1994), Chevalier and Sarazin (1994), Crawford et al. (1994, 1995), Crawford (1996), Field and Ferrara (1995), Mac Low and Zahnle (1994), Sekanina (1 993), Zahnle (1992), and Zahnle and Mac Low (1994) and has the following general characteristics as the fireball descends: a relatively slow initial rise, approximately proportional to the atmospheric density, reaching a maximum which is then followed by a rapid decrease below this peak. The physics of large impactor energy loss is poorly understood, but includes radiation, fragmentation, ablation, and lateral expansion. Models which include these effects to various (and often conflicting) degrees have been presented, and it is difficult to choose between them. In the spirit of our model, we adopt a simple physical description which mimics the expected overall deposition profile and includes ablation of cometary material into

the debris channel. In this model, the impactor velocity profile *V(s)* along the path is determined by the aerodynamic force *from* the atmosphere as

$$M\frac{dV}{ds} = \frac{1}{2}C_d A_0 \rho_a V(s) \qquad (17)$$

where M(t) is the mass of the fragment, C_d is the drag coefficient, and A_0 is the interaction area. As the fragment descends it loses mass through ablation; we assume here that the mass loss equals the mass of the interacting atmospheric gas, $dM/ds = \rho_a A_0$. *Thus, the* initial debris channel gas, half of which is cometary, has a density twice ambient. We assume an impactor density of $\rho_0 = 1$ and put $C_d = 1$, since the exact shape is unknown. For much of the entry path, lateral spreading is negligible (Field and Ferrara, 1995) so we equate the area A_0 to that of the fragment, $A_0 = \pi r_0^2$, and assume that this holds over the entire path. The energy deposition profile is then $\varepsilon(s) = \mathrm{M}\ VdV/ds + \left(V^2/2\right)dM/ds$, evaluated by numerical integration. This model, while simple and displaying the required overall characteristics, probably overestimates the penetration depth since lateral spreading increases the energy deposition rate over that assumed here.

Temporal evolution of the fireball is found by numerically integrating the axial and radial equations-of-motion, The Eulerian derivatives for axial motion are cast into ordinary partial derivatives of the variables $\hat{\rho}$, $\hat{p}$, and u and we compute at each time step $\partial\hat{\rho}/\partial t$, $\partial\hat{p}/\partial t$, and $\partial u/\partial t$, as well as c_s. The numerical scheme is pedestrian, employing the simple Euler method to find, for example, $u(t + \mathrm{At}) = u(t) + (\partial u/\partial t)\,At$. The time increment is made small enough such that halving it achieves the same result to good approximation. Numerical stability is obtained by performing a running, five-point, weighted, axial average on the newly computed set of values. Azimuthal variations are described by dividing the debris channel into quadrants. A value y = 1.2 is used throughout, based upon the results of the preceding section.

The calculation consists of two phases. The first is a "bolide" or meteor phase, where the fragment is descending into the atmosphere. At increments along the path (generally 0.2 km in vertical extent, or 1 / 100 of a scale height) the time development is computed for the altitudes above the fragment. When the impactor has lost most of its kinetic energy, we consider it to have stopped and compute the evolution of the “fireball” phase at time increments t = 2 msec and the same vertical resolution. Quantities computed include the debris channel density, pressure, radius, velocity, and temperature, the shock front location and velocity, the kinetic energy, radiated energy, work done on the atmosphere, and the instantaneous thermal energy. The altitude range of the calculations is typically from 400 km down to -200 km, depending on the impactor size (zero altitude is placed at the 1 bar level).

To compare these results to the observations, we find the color temperature and effective diameter in very much the same way as done with the measurements themselves. For altitudes above the ammonia cloud level, assumed here to occur at a pressure level of 500 mbar, we compute the source intensity at two wavelengths (2 and 4 μm), and from the ratio of these intensities we compute the effective color temperature. With this temperature estimate, the emitting area and effective diameter are found, exactly as done for the observations. We also compute the vertical source function (or contribution function) to illustrate where the emissions emanate.

VI. COMPARISONS AND DISCUSSION

Temperature and Effective Diameter

We have varied the single parameter - the diameter d_0 of the impactor - and computed the temperatures and areas (represented as the effective diameter D_{eff}) as would be seen from *Galileo*. We establish the time reference by assigning t = O to the instant when the calculated fireball temperature is 8000 K, the value deduced at the onset by the PPR and UVS measurements (see Fig. 4a and Section IV, Temperatures, Areas, and Effective Diameters).

Observed and theoretical temperatures are shown in Fig. 8a. The theoretical curves, referenced to the 8000"K PPR/UVS datum at t = O (which occurs when the fragment is at - 200 km) shows a rapid decrease. A minimum is attained - 3 sec later, with the subsequent rise in temperature attributed to the increased thermal capacity and slower cooling rates as the impactor descends. Similar features are found in some light curves computed by D. Crawford (private communication, 1996). At $t \approx$ 5 see, the impactor penetrates the cloud, producing the cusp seen in the Figure. For times less than 35 seconds, the theoretical curves and experimental data are consistent and suggest a diameter of d_o = 300 ± 100 m with a preference for the upper range. At times later than 35 seconds, the observed temperatures are consistently higher than predicted. This may be due, in part, to our approximation for the debris surface temperature, which ignored turbulent radial mixing between the hotter core of the debris channel and the cooler, denser radiating surface. Mixing would increase the temperatures from that computed, consistent with observations.

The corresponding diameter comparison is given in Fig. 8b, where the computed curves indicate that the change in expansion velocity hinted in Fig. 4b may be a real effect. The

computations show that the plateau and subsequent decrease in theoretical diameters D_{eff} arises from smaller axial velocities being produced at these later times, and depend upon the details of the energy deposition profile. The hot gas in the debris channel thus moves up more slowly so effective emission occurs at lower altitudes, where the debris channel radii are smaller. Even though the physical area of the entire fireball continues to increase, the effective luminous area reaches a maximum altitude and then slowly descends to regions where the debris channel is thinner. There is spectral evidence for this in the NIMS data, where absorption depths at later times show an increase (after reaching a minimum), suggesting a source which is decreasing in altitude. Examination of the effective diameter calculations with the observations suggests a fragment diameter of 200 to 300 m, or perhaps slightly higher.

The agreement between the fragment size determined from the temperature and that from the effective diameter data is quite satisfying and lends credence to the theoretical model. The possible errors in our determination are of two types. The first is the variance of the data about the assumed correct theoretical curves, while the second is the veracity of the theory itself. The latter is impossible to estimate without extensive comparisons with numerical simulations, which must also include radiative losses and the asymmetry of the atmosphere about the axis. A subjective look at Fig. 8 suggests uncertainties of about ± 100 m, since the temperatures are adequately fit by a 300-400 m fragment while the effective diameters could be consistent with a 200-300 m bolide. We therefore suggest that the G impactor was very approximately 300 * 100 m in diameter, but consider this a provisional estimate to be verified (or refuted) by comprehensive numerical simulations. Preliminary results from such simulations indicate a diameter for the G fragment of 370 m (D. Crawford, private communication, 1996). The energy and mass for our nominal 300 m case is 2.5 x 10^{26} erg and 1.4 x 1013 gm, respectively.

It is natural to inquire about the shape of the fireball and where the observed emissions originate. Some results are shown in Fig. 9, illustrating the shape and dimensions of the

fireball 26 seconds after our reference time, for the nominal 300 m case. This portrayal represents the view that was presented to *Galileo* and a spectrum obtained for this time period is shown in Fig. 3b. The location of the obscuring ammonia cloud deck is shown, and the altitude of peak energy deposition indicated, but this level is probably deeper than actually occurred since we have not included lateral expansion effects. For the time represented here, the debris front has a maximum width of -50 km which occurs at z = 220 km. The shock boundary projects a width of -110 km. The debris surface temperature profile and the source function (or contribution function) ***dS/dz*** for 3 μm radiation are also given (Fig. 9b) where one sees that the peak in the source function occurs at z = 130 km. The *source* function was derived using the assumption that the fireball is optically thick at all altitudes, an assumption that must break down when the debris channel has greatly expanded. However, in expansion these regions also cool, and contribute less to the total radiation even in the (assumed) optically thick case, so this assumption may not be crucial. Most of the observed radiation emanates from the altitude region 20 - 250 km. At the peak (130 km) the debris channel width is – 15 km. Proceeding downward from this peak, the debris surface temperature is still rising, but the width of the channel is decreasing more quickly than the increase in surface radiance. (The width in the drawing is not to scale for the lower altitudes.) The temperature of the fireball is estimated using the altitude-integrated source functions at 2 μm and 4 μm, integrating from the cloud top and above (i.e. just the solid portion of the *dS/dz* curve, Fig. 9b). The derived color temperature, $T \approx 1700$ K, is indicated. Axial and shock front velocities are also shown (Fig. 4C).

Fireball Energy Budget

The kinetic energy of the incoming fragment will reappear in various forms, as the many physical processes operate within the resulting fireball. These manifestations include thermal

energy, radiative losses, work done on the surrounding atmosphere in driving the outgoing shock wave, and the kinetic energy of debris channel mass flow. Energy histories are computed to ascertain the relative importance of the various processes and compare the radiation loss with that observed. The calculation is approximate, since the altitude range considered is finite and energy flows out the upper and lower boundaries, disappearing from the computational range.

The radiated power is computed as described above ($\hat{q}_{rad}$, Section V, Eq. 12) and integrated over time. At the same time we compute the radiative loss that occurs from the cloud top levels and above. The work performed on the atmosphere, $\hat{q}_{pdV}$ (Eq. 11) is likewise summed over time. The energy of axial flow is computed as the distance and time integral of $-A_d \nabla \hat{p} \cdot u$, while the thermal energy is computed at each time step as the path integral of $\hat{p}/(\gamma - 1)$. Results for our nominal impactor size are presented in Fig. 10.

From the Figure, it can be seen that the initial energy deposition is in thermal energy and radial expansion, as expected. During the first 10 seconds of the period shown the fragment is still descending and losing energy. At the termination of this travel, there is no more thermal energy input and this energy is at its maximum. Initial losses of thermal energy are radiative and work done on the external surroundings - the atmosphere. Radial expansion is rapid at first, with most of this energy component quickly attained. During the 10 seconds of bolide phase shown here, the radiative loss is also rapid, as shown by the relatively greater slope of the radiative loss curve. This radiation is emitted below the cloud deck (for our simple energy deposition profile). During the fireball phase, the radiation source moves up in the atmosphere, and eventually most of it is radiated from above the clouds (cf. Fig. 9). The energy of axial motion increases more slowly, and never attains the magnitude of the radiated loss and atmospheric work. R is this component that provides the energy for the splash phase

phenomona, ultimately appearing as radiation (primarily) during and following the splashback. The radial kinetic energy in the debris channel is always a small component.

In an earlier Section (IV, Temperatures, Areas, and Effective Diameters), a zeroth-order energy estimate of 5 x 10^{25} erg was found for the outgoing shock component of the total energy From Fig. 10, this component is - 1/2 of the total, so this zeroth-order estimate suggests a total energy of -1 x 10^{26} erg, in fair agreement with the energy (2.5 x 10^{26} erg) associated with our nominal 300 m diameter impactor.

The integrated luminosity that was derived in Section IV from the observed temperatures and area can be compared to the above-cloud radiated energy curve shown in Fig. 10. The observed value (0.48*0. 13 x 1025 erg) is about a factor of two lower than the predicted value (1.0 x 10^{25} erg), again demonstrating fair agreement.

Velocities and Mass Outflow

A quite striking result of the Shoemaker-Levy 9 phenomena was the high altitude plumes, and the fact that they all seemed to reach approximately the same height. From Hubble Space Telescope results (Hammel et al., 1995) the G plume reached –3300 km (above the 100 mbar level) which infers a vertical velocity component of $v_{\perp}$ = 13 km see^{-1}. If the debris channel axis is inclined at θ_0 = 45 deg, then axial velocities of $u \approx$ 18 km see^{-1} are necessary. It is of interest to compare our results with the velocities required by the plume heights. Before doing so, let us perform the following simple calculation, which addresses the invariant plume height question.

Imagine that we have an impactor of energy $E_0 = 1 / 2M_0V_0^2$ depositing its energy over a scale height H, and that the energy deposition profile is linear. The force per unit distance due to the pressure gradient is therefore constant over the interval and of magnitude $(\gamma - 1)M_0V_0^2 / H$. The total force acting over the scale height is this quantity times H. If the accelerated mass is twice the impactor mass (i.e. equal amounts of cometary and Jovian material), and if the force operates over an effective distance H as the mass is accelerated up, then the kinetic energy is $1/2(2M_0)u^2 = (\gamma - 1)M_0V_0^2$. Thus, $u \approx \sqrt{\gamma - 1}\, V_0$, to within a numerical constant of order unity, and is independent of the initial mass or the specific atmospheric structure. For $\gamma = 1.2$, we find $u \approx 27$ km see-1, discounting radiative and other energy losses.

Numerical results for the axial velocity evaluated at 400 km altitude and for our nominal case are shown in Fig. 11. We also show the corresponding mass outflow, which will appear in the splash phase several minutes later. The velocity is fairly constant, with almost zero mass outflow, for the first 30 seconds, at which time there is an abrupt increase in both quantities. The velocity reaches a maximum of u .22 km see-l at $t \approx 40$ see, with the maximum mass outflow occurring a few seconds earlier. The mass flow is sharply peaked, suggesting shock-like axial flow. At the time of the maximum outflow, the axial velocity is $u \approx 17$ km see-l.

These velocities are somewhat higher than that required for 3300 km plume heights. It is plausible that the material producing the visible plumes is derived from depth, and emerges at $t \approx 60$ see, when $u \approx 18$ km see-1. Viscous interactions with thermospheric gas could also play a role, slowing down the material, as well as simply more radiative loss from the fireball, which reduces the pressure and its gradient, decreasing the velocities. The mass outflow, integrated over the computed time, is -2.2 x 1013 gm. The relative Jovian and cometary contributions are equal in this model, giving 1.1 x 1013 gm from cometary origin. If 40°/0 of this mass produces water in the splash-phase shock (Zahnle et al., 1995, Model WC), then our calculations predict a value (4.4 x 1012 gm) which is comparable to the water abundance

observed by Bjoraker et al. (1996) and Encrenaz et al (1997) for the G splash. The mass of water found from Bjoraker et al.'s Kuiper Airborne Observatory measurements of the splashback area is 1.4 - 2.8 x 1012 gm, which they consider lower limits to the total amount of water in the G splashback. Encrenaz et al., using NIMS data, found 0.6 - 2.9 X 10^{12} gm at 9 minutes after the impact.

Although the amount of splash-phase water predicted for a 300 m impactor is consistent with observations, the amount of carbon monoxide found by Lellouch et al. (1995) is not. They observed microwave fluxes corresponding to 1 X 10^{14} gm of CO. In the best case, this is a factor of five more oxygen than provided by a 300 m comet; in realistic cases the ratio would be a factor of ten. We therefore regard our derived size as a lower limit.

Opacity Sources

in all of the above, we have assumed that the fireball behaves as a blackbody, but have not considered the mechanisms that produce the opacity. The spectra shown in Fig. 3 indicate that the Planck function fits the observations quite well for the four NIMS continuum wavelengths (1 .84 to 4.38 pm), as well as for the PPR bandpass at shorter wavelengths (0.945 μm). The fits are good over a wide temperature range. If the emissivity was a strong function of wavelength, a good fit might be obtained for a limited temperature range, but likely not all, suggesting that the emissivity is, at most, a slowly varying function of wavelength. Since the absorption cross section for most processes is wavelength-dependent, a nearly constant emissivity requires that the medium be optically thick.. This condition will produce near-unit emissivity, which has been assumed in all of this work.

At high temperatures, the low-ionization-potential metals provided by the comet (Ross-Serote et al., 1995; Weaver et al., 1995) will produce copious amounts of electrons, as will chemi-ionization processes (Gaydon and Wolfhard, 1970, pp. 325-328) which can then produce infrared emissions through free-free transitions with negative ions (H^-, He^-, C^-, O^-, C_2^-, etc.) and through free-bound radiative recombination into Rydberg levels. While an accurate calculation of the emission rate, or the corresponding opacity, has not been performed here, it is probably safe to say that these become inefficient processes by the time the temperature has dropped to 3000 K. Nevertheless, the spectra show blackbody behavior for temperatures well below this. Some other opacity source was operating. In the following, we speculate on some possible sources.

We find a possible clue in the behavior of familiar high temperature gases - flames - where continuum blackbody radiation arises from particles, generally carbon particles, which are produced in the flames. Soot happens! (K. Zahnle, private communication, 1995.) Let us consider the possibility of carbon particles in the fireball. We take, as our reference for this and subsequent calculations, the fireball conditions for t = 26 sec at the altitude ($z \approx 130$ km) where the 3 μm source function is a maximum, shown in Fig. 9. At this level and time, the mass per unit length is $\hat{\rho}$ = 450,000 grams cm^{-1} and the pressure is $p \approx 8$ mb, approximately four times the external atmospheric pressure. The debris surface temperature at this altitude is T_d = 1686 K, and the average radius is $\langle r_d \rangle \approx 15$ km. Prior to this time, this parcel of gas was at a higher temperature, at which carbon could have started condensing. The presence of charged particles greatly enhances the formation of condensation centers, and such ions will be produced by thermal ionization of Na, K, and others, as well through quenching of a higher temperature ionization state (Raizer, 1960). The amount of carbon gas available to condense can be estimated from the work of Borunov et al. (1996), They find, for a uniform, equal mixture of Jovian and cometary gas (by mass, the same assumption used in our model), that volume mixing ratios of ~10-3 are produced in the early fireball, and decrease with time. A

similar value would be found in the Jovian fraction if the two contributions were not well mixed. Using the mass density for this parcel, and assuming that all of the free carbon condenses, then with the complex indices of refraction measured by Roush (1995), and for the average radius $\langle r_d \rangle$ we find an optical depth of $\tau \approx 3$ at a wavelength of 3 μm We use the small particle approximation and the electrical dipole moment contribution to the absorption efficiency: $Q_{abs} = (2\pi a/\lambda)$ 9 where a is the particle radius and with $n + ik$ for the complex index of refraction, g = $24nk/\left[(n^2 - k^2 + 2)^2 + (2nk)^2\right]$ (Landau and Lifshitz, 1984), §§. 83, 93). This opacity is independent of particle sizes, so long as they are small. Since we have assumed that all of the free carbon condenses, and have ignored reactions of atomic oxygen and water vapor with the particles (which would act to destroy the particle through CO production), it seems unlikely that carbon particles provide the opacity of the fireball.

At temperatures of about 3000 K, the refractory metal oxides will begin condensing. The most important of these is MgO, with melting point MP = 3100 K and boiling point BP = 3466 K (both at atmospheric pressure; the values will be somewhat lower for the partial pressures here). Hot magnesium oxide particles, as produced in the laboratory by burning Mg, is an efficient radiator producing an intense white continuum, but the emissivity of the individual particles is not known. At room temperature, magnesia is not very absorbing at visible and near infrared wavelengths, but band shifts and strength changes can occur at high temperatures. More importantly, the presence of impurities, as is likely to occur considering the diverse gas composition, can drastically alter the optical properties. For lack of specific information, we will estimate the magnitude of the opacity using simply the geometric cross section. For conditions as noted above, and using a particle radius of a = 1000 A, we find an optical depth of $\tau \approx 30$. This suggests that hot, impure MgO particles maybe one component of the opacity.

For somewhat lower temperatures, iron will condense as a liquid (MP = 1808 K, BP = 3273 K), along with Ni (and perhaps Si) to form an alloy. Raizer (1960) has considered the condensation

of iron in the impact explosion of an asteroid, finding that Fe particles of radius a = ***3000*** A are produced as the gas expands into a vacuum. With this radius, the iron content of Anders and Grevesse's (1989) compilation, and the indices of refraction of Lynch and Hunter (1991), the 3 μm opacity due to iron is $\tau \approx 10$. Here, because of the large n and k values, it is appropriate to use the magnetic dipole term for the absorption efficiency: Q_{abs} ***=(4nk/15)(2mz/L)'.*** Condensed Fe is a potential candidate for one contributor to the opacity source.

At lower (but still high) temperatures, SiO_2 condenses (MP = 1996 K, BP = 2500 K). Impurities such as Fe^{++} and OH are likely to be present, enhancing the absorptive properties of silica particles. Again, without more information, we quantify the magnitude of the opacity using the geometric cross section. At our standard conditions, and for particles of 1000 A radius, we find an optical depth of $\tau \approx 100$. An emissivity estimate can be obtained from the infrared reflectance of a fine -grained, optically-thick layer of quartz (Salisbury et al, 1991) and lunar glass (Wells and Hapke, 1977), for which the diffuse reflectance was found to be - 10-20'% in the 1-5 μm region. From this we estimate emissivites of -0.8 - 0.9. The addition of mafic impurities to produce basaltic glass will raise the emissivity to -0.9-0.95 if the Salisbury et al. (199 1) olivine reflectance serves to represent the addition of iron. We submit that SiO_2 seems quite promising as an opacity source.

As time progresses and the fireball cools further, it is probable that the three latter particle types could coalesce, producing the ferromagnesium silicates olivine and pyroxene. Indeed, silicates have been identified in the splash phase of the R event (Nicholson et al., 1995).

Finally, we should consider absorption by water vapor. H_2O has several bands in the near infrared, close to the observed continuum wavelengths. As a naive estimate, we take the cometary oxygen fraction remaining after forming carbon monoxide, and assume that it produces water vapor. With this mass, and using the absorption values computed by Auman

(1967), we find an optical thickness at 3 μm of $\tau \approx$ 0.09-0.36, depending upon the turbulence velocity. Hot water, therefore seems unlikely as a major opacity source. One could assume that the impactor mass was a factor of 10 times greater, which would then produce near-unit optical depth (or greater) for all four of our wavelengths, but the opacity at the PPR wavelength (which is consistent with unit emissivity, see Fig. 3) would still be too low. We find 7(0.945 μm) -0.01 in this 10 x higher mass case. Furthermore, the water vapor mixing ratios computed by Borunov et al. (1996) are much lower than our above assumption, except for their models 4A and 4B, which include Jovian water, and even then water mass would be comparable to our first estimate.

To summarize, we suggest that the opacity of the fireball is caused by the refractory particles MgO, Fe, and SiO_2 and, at lower temperatures, the silicate minerals that can be formed from them. These particles will contribute to the ejects material so prominent on Jupiter after the impacts.

VII. SUMMARY

The favorable position of the *Galileo* spacecraft, then enroute to Jupiter, provided us a direct view of the Shoemaker-Levy 9 collision events, and the NIMS observations of the G event are discussed here. This analysis concentrates on the temperature, size, and associated energy of the initial phase - the fireball. Three main categories are presented; the first is a discussion of the observations, giving the experimental aspects of the measurements, the analysis methods, and the primary, model independent results (Sections H, 111, and IV, respectively). The second category is the development of a simple, heuristic theory which can describe the fireball phenomena (Section V). We then compare the observational data with this theory and find a provisional estimate of the G impactor mass (and energy) and show the size, velocity, and energy history of the fireball (Section VI).

The observations were performed at five second temporal resolution in 17 discrete, narrow wavelength bands, but only ten of these are useful for fireball characterization. These wavelengths span the near infrared range, and four of these bands, at 1.84, 2.69, 2.97, and 4.38 μm, are continuum channels which we use for temperature estimation. Instrumental characteristics for point source measurements are discussed, leading to the spectroradiometric evaluation of the luminous source intensity, the power emitted per unit wavelength and solid angle. These values are corrected for reflection by the underlying Jovian clouds using albedos derived with the same instrument. The errors that are introduced by intrinsic instrumental noise and by pointing variances (jitter) are analyzed. The mean signal-to-noise ratio, after subtracting the reflected solar flux component of the signals, is found to be - 7:1.

The light curves at these four wavelengths show that the G fireball lasted about one minute, as observed in the near infrared. recognizable NIMS signals are found five seconds after the onset

observed by the *Galileo* PPR and UVS instruments (Martin et al., 1995, Herd et al., 1995). The duration of the signals increases with increasing wavelength, surely due to the temperature of the fireball decreasing as it expands.

Temperatures were obtained by fitting a Planck function to the source intensities at the four above-mentioned continuum channels. The analysis method minimizes χ^2, finding the best fitting temperatures and amount of reflected solar flux. Temperatures vary from T ≈ 3000 K at the beginning to T ≈ 1000 K after one minute. A semi-empirical adiabatic expansion law obtained with the area measurements (see below) shows consistency with the PPR/ UVS derived temperature (T ≈ 8000 K) found at the onset.

The emitting areas (and effective diameters of the equivalent sphere) *were* found using the temperatures and absolute values of the source intensities, assuming unit emissivity. The area varies from 400 to 20,000 km^2, and the corresponding diameters are 23 to 160 km. The effective diameter seems to increase at the rate of 3.2 km sec^{-1} during the first 45 seconds. Beyond that time, the behavior is unclear, due to the uncertainties in our area determinations. Although the physical area projected by the fireball continues to increase, it is likely that the effective luminous area reaches a maximum and then actually decreases. The cause of this behavior may be the slower ascent (axial) velocities found for this time period by the model.

Assuming that the derived temperatures and diameters represent a suitable average, we have used these data to estimate the adiabatic index. Two methods were used for this estimation. In the first method, the logarithmic slope of the temperature and inferred volume relationship was employed, giving a value of $\gamma = 1.2 \pm 0.1$. The second method, which gives nearly the same result, used the temperature at the time of the maximum in the light curves for different wavelengths. These estimates are in good agreement with expected values of the adiabatic index.

A very crude estimate of the fireball energy was derived by assuming that the absorption features in the spectrum correspond to shock entrained Jovian atmosphere gas. From the depths of the bands, and using the velocity and size of the fireball, an energy of 5 x 1025 erg was found. The luminosity, when integrated over the first minute of the event and assuming isotropy, gives an above-cloud radiative energy loss of $0.48 \pm 0.13 \times 10^{25}$ erg.

In order to describe the fireball phenomena more completely we then develop a simple heuristic theory of its early stages. We envision that the entering fragment produces a wake of very hot gas, for which half of the mass is from ablated cometary material. This energetic gas, initially twice as dense as the ambient atmosphere (by assumption) has an internal pressure many times greater than the exterior. The surface of this channel, which we call the debris channel, then rapidly expands and drives an outgoing radial shock. At the same time, the pressure gradient along the channel accelerates the debris gas back along the entry path, so the radial shock is driven by a time-varying energy as matter moves along the channel. We assume that the debris introduced by the comet produces an optically thick debris surface, introducing radiative losses and producing the emission observed by NIMS. Axial velocities are found by solving (numerically) the equations-of-motion for one dimensional flow with variable area. The radial motion is computed concurrently using the instantaneous pressure differential between the debris channel and the atmosphere. From the calculated shock velocities we find the shock radius and using Sedov's (1959) theory, we obtain the velocity and radius of the debris front. Axial and radial motions are coupled through the work done on the atmosphere - the kinetic and thermal energy of the outgoing shocked Jovian gas. The debris surface temperature is assumed to be proportional to the thermal energy content, with the initial value consistent with entry shock heating. This simple theory has only just parameter, the size of the incoming fragment, assumed to be of unit density.

The comparison of our observations and this rudimentary theory is fair, at least for the first half of the fireball phase. The computed temperature-time profiles suggest that the G impactor had a diameter of between 300 and 400 m, while the area (effective diameter) comparison suggest diameters between 200 and 300 m. We suggest provisionally a diameter of 300 ± 100 m from the (assumed unit density) G fragment, but regard this more as a lower limit than an accurate size determination. More precise estimates must await detailed numerical simulations by others.

Energy apportionment in the developing fireball was also computed, including the total above-cloud integrated luminosity. For the nominal impactor size, the observed and theoretical luminous energy values agree to within a factor of two. Axial velocities found from the theory are slightly higher than those required to produce the observed high altitude plumes (Hammel et al., 1995). The model's estimate of the water mass in the splashback is within a factor of three (or better) of the measurement by Bjoraker et al. (1995) and Encrenaz et al. (1997), but the amount of CO found by Lellouch et al. (1995) is larger, by approximately a factor of ten, than that allowed in the model.

We have investigated the opacity sources which produce the measured luminosity, and speculate that high temperature particles - condensed MgO, Fe-Ni, and SiO_2, probably with impurities - can provide the opacity.

Future work on our part will include analysis of the absorption feature of the spectra,, and comparison with the R impact data. Refinements of the model are also possible, and the behavior for different fragment densities and for different ratios of comet and atmospheric mass are worth exploring. We encourage continued numerical simulations of fireball phenomena.

ACKNOWLEDGMENT

We gratefully acknowledge and thank Kevin Zahnle for insightful comments and discussion, and for uncovering blunders in the original draft. We also thank Dave Crawford for discussions, correspondence, and for sharing his numerical simulation data with us. His demonstration that the fireball area varied with impactor size prompted us to pursue our heuristic model. Thanks also to Frank Leader and Bob Mehlman for expertly processing the original data records, and to the Galileo Project Management team (Bill O'Neil, Neal Ausman, and Bob Mitchell) for support. Portions of this work were performed at the Jet Propulsion Laboratory, California Institute of Technology, under a contract with the National Aeronautics and Space Administration.

REFERENCES

Ahrens, T.J., T. Takata, J.D. O'Keefe, and G.S. Orton 1994. Impact of Comet Shoemaker-Levy 9 on Jupiter. *Geophys. Res. Lett.* 21, 1087-1090.

Anders, E., and N. Grevesse 1989. Abundances of the elements: Meteoritic and Solar. *Geochim. Cosmochim. Acts* 53, 197-214.

Auman, J. Jr. 1967. The infrared opacity of hot water vapor. *Astrophys. J. Suppl. Ser. 14, 171-206.*

Bevington, P.R. 1969. *Data Reduction and Error Analysis for the Physical Sciences.* McGraw-Hill Book Company, New York.

Bjoraker, G. L., S.R. Stolovy, T.L. Herter, G.E. Gull, and B.E. Pirger 1996. Detection of water after the collision of fragments G and K of Comet Shoemaker-Levy 9 with Jupiter. *Icarus* 121, 411-421.

Borunov, S., P. Drossart, and Th. Encrenaz 1997. High temperature chemistry in the fireballs formed by the impacts of comet P/Shoemaker-Levy in Jupiter. *Icarus.* 125, 121-134.

Boslough, M. B., D.A. Crawford, A.C. Robinson, and T.T. Trucano 1994. Mass and penetration depths of Shoemaker-Levy 9 fragments from time-resolved photometry. *Geophys. Res. Lett.* 21, 1555-1558.

Boslough, M. B., D.A. Crawford, T.G. Trucano, and A.C. Robinson 1995. Numerical simulations of the Shoemaker-Levy 9 impacts as a framework for interpreting observations. *Geophys. Res.* Lett. 22, 1821-1824.

Carlson, R. W., P.R. Weissman, W.D. Smythe, and J.C. Mahoney, 1992. Near-infrared mapping spectrometer on Galileo. *Sp. Sci. Rev.* 60, 457-502.

Carlson, R. W., P.R. Weissman, M. Segura, J. Hui, W.D. Smythe, T.V. Johnson, K.H. Baines, P. Drossart, Th. Encrenaz, and F.E. Leader 1995a. *Galileo* infrared observations of the Shoemaker-Levy 9 G impact fireball: a preliminary report. *Geophys. Res. Lett.* 22, 1557-1560.

Carlson, R. W., P.R. Weissman, J. Hui, M. Segura, W.D. Smythe, K.H. Baines, T.V. Johnson, P. Drossart, T. Encrenaz, F. Leader, and R. Mehlman 1995b. Some timing and spectral aspects of the G and R collision events as observed by the *Galileo* near infrared mapping spectrometer. *Proceedings of the European SL-9 Workshop,* Ed. by R. West and H. Bohnhardt, 69-73.

Carlson, R.., W. Smythe, K. Baines, E. Barbinis, K. Becker, R. Burns, S. Calcutt, W. Calvin, R. Clark, G. Danielson, A. Davies, P. Drossart, T. Encrenaz, F. Fanale, J. Granahan, G. Hansen, P. Herrera, C. Hibbits, J. Hui, P. Irwin, T. Johnson, L. Kamp, H. Kieffer, F. Leader, E. Lellouch, R. Lopes-Gautier, D. Matson, T. McCord, R. Mehlman, A. Ocampo, G. Orton, M. Roos-Serote, M. Segura, J. Shirley, L. Soderblom, F. Taylor, J. Torson, A. Weir, and P. Weissman 1996. Near Infrared Spectroscopy and Spectral Mapping of Jupiter and the Galilean Satellites: Results from Galileo's Initial Orbit. *Science 274, 385-388.*

Chevalier, R. A., and C.L. Sarazin 1994. Explosions of infalling comets in Jupiter's atmosphere. *Astrophys. J. 429, 863-875.*

Crawford, D. A., M.B. Boslough, T.G. Trucano, and A.C. Robinson 1994. The impact of Comet Shoemaker-Levy 9 on Jupiter. *Shock Waves 4, 47-50.*

Crawford, D. A., M.B. Boslough, T.G. Trucano, and A.C. Robinson 1995. The impact of periodic Comet Shoemaker-Levy 9 on Jupiter. *Int. J. Impact Engng.* 17, 253-262.

Crawford, D.A. 1996. Models of fragment penetration and fireball evolution. *The Collision of Comet Shoemaker-Lay 9 and Jupiter.* Ed. by K. S. Nell, H. A. Weaver, and P. D. Feldman. Cambridge University Press, Cambridge.

Drossart, P. and Th. Encrenaz 1983. The Jovian spectrum in the 3-yin window. *Icarus 55, 390-398.*

Drossart, P., T. Encrenaz, B. Bezard, J.-P. Maillard, and R. W. Carlson 1997. Interpretation of CH_4 emissions during the splash phase of R-impact from CFHT/FTS and NIMS/Galileo observations. *Planet. Sp. Sci.* (in press).

Encrenaz, Th., P. Drossart, R. W. Carlson, and G. Bjoraker 1997. Detection of H_2O in the splash phase of G-impact from NIMS-Galileo 1997. *Planet. Sp. Sci.* (in press).

Field, G. B., and A. Ferrara 1995. The behavior of fragments of Comet Shoemaker-Levy 9 in the atmosphere of Jupiter. *Astrophys. J. 438, 957-967.*

Gautier, D., B. Bezard, A. Marten, J.P. Baluteau, N. Scott, A. Chedin, V. Kunde, and R. Hanel 1982. The C/H ratio in Jupiter from the Voyager infrared investigation. *Astrophys. J. 257, 901-912.*

Gaydon, A. G., and H.G. Wolfhard 1970. *Flames*. Chapman and Hall, London

Hammel, H. B., R.F. Beebe, A.P. Ingersoll, G.S. Orton, J.R. Mills, A.A. Simon, P. Chodas, J.T. Clarke, E. De Jong, T.E. Dowling, J. Barrington, L.F. Huber, E. Karkoschka, C.M. Santori, A. Toigo, D. Yoemans, and R.A. West 1995. HST imaging of atmospheric phenomena created by the impact of Comet Shoemaker-Levy 9. *Science 267,* 1288-1296.

Ginzburg, I. P. 1963. *Applied Fluid Dynamics*. NASA Technical Translation TT F-94, U.S. Dept. of Commerce, Washington DC.

Herd, C. W., W.R. Pryor, A.I. F. Stewart, K.E. Simmons, J.J. Gebben, C.A. Barth, W.E. McClintock, and L.W. Esposito 1995. Direct observations of the Comet Shoemaker-Levy 9 fragment G impact by *Galileo* UVS. *Geophys. Res. Lett* 22, 1565-1568.

Husson, N., A. Chedin, N.A. Scott, D. Bailly, G. Graner, N. Lacome, A. Lévy, C. Rosetti, G. Tarrago, C. Camy-Peyret, J.M. Flaud, A. Bauer, J.M. Colmont, N. Monnanteuil, J.C. Hilico, G. Pierre, M. Loete, J.P. Champion, L.S. Rothman, L.R. Brown, G. Orton, P. Varanasi, C.P. Rinsland, M.A.H. Smith, and A. Goldman 1986. The GEISA spectroscopic line parameters data bank in 1984. *Ann. Geophys. 86A, 185-190.*

Jessberger, E. K., A. Christoforidis, and J. Kissel 1988. Aspects of the major element composition of Halley's dust. *Nature 332, 691-695.*

Karkoschka, E. 1994. Spectrophotometry of the Jovian Planets and Titan at the 300- to 1000-nm wavelength: The methane spectrum. *Icarus* 111, 174-192.

Landau, L. D., and E.M. Lifshitz 1959. *Fluid Mechanics*. Pergamon Press, Oxford.

Landau, L. D., and E.M. Lifshitz 1980, *Statistical Physics*, Part 1. Pergamon Press, Oxford.

Landau, L. D., and E.M. Lifshiz 1984. *Electrodynamics of Continuous Media*. Pergamon Press, London.

Lellouch, E., G. Paubert, R. Moreno, M. C. Festou, B. Bézard, D. Bockelee-Morvan, P. Colom, J. Crovisier, T. Encrenaz, D. Gautier, A. Marten, D. Despois, D. F. Strobel, and A. Slevers 1995. Chemical and thermal response of Jupiter's atmosphere following the impact of comet Shoemaker-Levy 9. *Nature 373, 592-595.*

Liepmann, H. W. and A. Roshko 1957. *Elements of Gas Dynamics*. John Wiley and Sons, New York.

Lynch, D. W., and W.R. Hunter 1991. An introduction to the data for several metals. In *Handbook of the Optical Constants of Solids,* Ed. by E.D. Palik, Academic Press, New York.

Mac Low, M-M., and K. Zahnle 1994. Explosion of Comet Shoemaker-Levy on entry into the Jovian atmosphere. *Astrophys. J. 434, L33-L36.*

Martin, T. Z., G.S. Orton, L.D. Travis, L.K. Tamppari, and I. Claypool 1995. Observation of Shoemaker-Levy Impacts by the *Galileo* Photopolarimeter. *Science 268, 1875-1879.*

McGregor, P. J., P.D. Nicholson, and M.G. Allen 1996. CASPIR observations of the collision of Comet Shoemaker-Levy 9 with Jupiter. *Icarus* 121, 361-388.

Meadows, V., D. Crisp, G. Orton, T. Broke, and J. Spender 1995. AAT IRIS observations of the SL 9 impacts and initial fireball evolution. *Proceedings of the European SL-9 Workshop,* Ed. by R. West and H. Bohnhardt, 129-134.

Nicholson, P. D., P. J. Gierasch, T. L. Hayward, C. A. McGhee, J. E. Moersch, S. W. Squires, J. Van Cleve, K. Mathews, G. Neugebauer, D. Shupe, A. Weinberger, J. W. Miles, and B. J. Conrath 1995. Palomar observations of the R impact of comet Shoemaker-Levy 9:II. Spectra. *Geophys. Res. Lett.* ***22,1617-1620.***

Nell, K. S., H. A. Weaver, and P. D. Feldman, (Editors) 1996. *The Collision of* Comet *Shoemaker-Levy 9 and Jupiter,* Cambridge University Press, Cambridge.

Orton, G.S. 1981. Atmospheric structure in the equatorial region of Jupiter. *Galileo* Document No. 1625-125, Jet Propulsion Laboratory, Pasadena.

Raizer, Yu. P. 1960. Condensation of a cloud of vaporized matter expanding in vacuum. *Sov. Phys. JETP 37, 1229-1235.*

Roos-Serote, M., A. Baric, J. Crovisier, P. Drossart, M. Fulchignoni, J. Lecacheux, and F. Roques 1995. Metallic emission lines during the impacts of comet P/Shoemaker Levy 9 in Jupiter. *Geophys. Res. Lett.* 22, 1621-1624.

Roush, T.L. 1995. Optical constants of amorphous carbon in the mid-IR (2.5-25 μm, 4000-400 cm^{-1}). *Planet. Space Sci. 43, 1297-1301.*

Salisbury, J. W., L.S. Walter, N. Verge, and D.M. D'Aria 1991. *Infrared (2. 1-25pm) Spectra of Minerals.* The Johns Hopkins University Press, Baltimore.

Sedov, L. I. 1959. *Similarity and Dimensional Methods in Mechanics*. Academic Press, New York.

Sekanina, Z. 1993. Disintegration phenomena expected during the forthcoming collision of Periodic Comet Shoemaker-Levy 9 with Jupiter. *Science 262, 382-387.*

Shoemaker, E. M., P.J. Hassig, and D.J. Roddy 1995. Numerical simulation of the Shoemaker-Levy 9 impact plumes and clouds: A progress report. *Geophys. Res. Lett.* 22, 1825-1828.

Stanyukovich, K. P. 1960. *Unsteady Motion of Continuous Media*. Pergamon Press, New York.

Strecker D. W., E.F. Erickson, and F.C. Witteborn 1979. Airborne stellar spectrophotometry from 1.2 to 5.5 microns: absolute calibration and spectra of stars earlier than M3. *Astrophys. J. Suppl. Series 41, 501-512.*

Strong, K., F.W. Taylor, S.B. Calcutt, J.J. Remedies, and J. Ballard 1993. Spectral parameters of self- and hydrogen-broadened methane from 2000 to 9500 cm^{-1} for remote sounding of the atmosphere of Jupiter. *J. Quant. Spectrosc. Radiat. Transfer 50, 363-429.*

Takata, T., J.D. O'Keefe, T.J. Ahrens, and G.S. Orton 1994. Comet Shoemaker-Levy-9: Impact on Jupiter and plume evolution. *Icarus* 109, 3-19.

Weaver, H. A., M.F. A'Hearn, C. Arpignay, D.C. Boyce, P.D. Feldman, S.M. Larson, P. Lamy, D.H. Levy, B.C. Marsden, K.J. Meech, K.S. Nell, J.V. Scotti, Z. Sekenina, C.S. Shoemaker, E.M. Shoemaker, T.E. Smith, S.A. Stern, A.D. Storrs, J.T. Trauger, D.K. Yeomans, and B. Zellner 1995. The Hubble Space Telescope (HST) Observing Campaign on Comet Shoemaker- Levy 9. *Science 267, 1282-1288.*

Wells, E., and B. Hapke 1977. Lunar soil: iron and titanium bands in the glass fraction. *Science 195, 977-979.*

Wyatt, C.L. 1978. *Radiometric Calibration: Theory and Methods.* Academic Press, New York

Zahnle, K. 1992. Airburst origin of dark shadows on Venus. *J. Geophys. Res.* 97, 10, 243-10, 255.

Zahnle, K. and M.-M. Mac Low 1994. The collision of Jupiter and Comet Shoemaker-Levy 9. *Icarus* 108, 1-17.

Zahnle, K., M.-M. Mac Low, K. Lodders, and B. Fegley Jr. 1995. Sulfur chemistry in the wake of Comet Shoemaker-Levy 9. *Geophys. Res. Lett. 22, 1593-1596.*

Zel'dovich, Ya. B. and Yu. P. Raizer 1966. *Physics of Shock Waves and Hgh Temperature Hydrodynamic Phenomena, Vol. 1.* Academic Press, New York.

Table 1

Wavelengths and Derived Geometric Albedos

Detector	Wavelength μm	Wavenumber cm^{-1}	Geometric Albedo a_g	Absorber/Emitter	Notes
1	0.71	14,170	0.478	continuum	large
2	0.85	11,760	0.380	H_2 (T,weak)	Jovian
3	1.01	9,950	0.109	CH_4 (T)	reflected
4	1.28	7,790	0.275	continuum	sunlight
5	1.56	6,400	0.265	continuum	component
6	1.84	5,430	0.047	CH_4 (T)	continuum (S)
7	2.12	4,710	0.003	Hz (S)	
8	2.40	4,160	0.000	CH4 (S)	
9	2.69	3,710	0.206	H_2O (T)	continuum (S)
10	2.97	3,370	0.019	NH3 (T)	continuum (S)
11	3.25	3,080	0.002	CH_4 (S)	
12	3.53	2,830	0.002	H_3^+, CH4 (S)	
13	3.82	2,620	0.004	CH_4 (S)	
14	4.10	2,440	0.056	CH_4 (S,weak)	
15	4.38	2,280	0.023	PH3 (T)	continuum (S)
16	4.67	2,140		PH3 (T)	thermal
17	4.95	2,020		H_2O (T)	emission

Notes: The NIMS spectral bandpass is 0.025 μm for Detectors 3-17 (first order), and 0.013 μm for Detectors 1 and 2 (second order). S = Stratosphere, T = Troposphere.

FIGURE CAPTIONS

Fig. 1. Light curves for the four continuum wavelengths: 1.84 μm (a), 2.69 μm (b), 2.97μm (c), and 4.38 μm (d). Also shown (e) are the UVS and PPR light curves, as well as other G event timings. The source intensities are expressed in $TW\ ster^{-1}\ \mu m^{-1}$ and have been corrected for cloud reflection. Note that the duration of the signals increases with wavelength. The splash phase, commencing six minutes later, is not shown. The reference time $t = O$ corresponds to 07:33:32 UTC on 18 July 1994 (Day 199), derived from the spacecraft time of the initial rise of the PPR signal (Martin et al., 1995). The UVS onset (Herd et al., 1995) may have occurred up to one second earlier. The NIMS measurement at $t = -0.8$ sec shows no significant enhancement above the noise level although the source may have been too small to give a measurable signal. A weak high-altitude emission feature was captured in a Hubble image taken in the interval 07:33: 16–46 (Hammel et al., 1995) and is presumably the entry meteor flash. The first and second precursors (PC] at 07:33:08, PC2 at 07:35:00) found by McGregor et al. (1996) are shown. They are identified respectively with the high altitude entry meteor flash and thermal emission from the fireball as it rises above the limb. McGregor et al. also observed leader emissions at 07:32:20, perhaps due to a preceding dust cloud associated with the G fragment. Measurements at 2.3 μm using the Anglo-Australian Telescope (AAT, Meadows et al., 1995) also show an early, possibly dust related event starting at 07:32:58 The noise in the NIMS measurements is due to intrinsic instrumental noise and variations in the spatial response coupled with the slightly different pointing conditions of each spectrum. The curious and seemingly systematic intensity alternation in (a) correlates with spacecraft scan-platform direction (only). It's cause is not fully explained.

Fig. 2. Spatial scan pattern for the impact observations and NIMS angular sensitivities. The time sequence and spatial arrangement of pixels is shown, with the relative size of Jupiter

indicated. The path of the comet fragments and impact location is also shown. NIMS internal mirror scanning (cross-cone direction) produces a vertical column or stripe of twenty pixels, for which we show the central four pixels for three successive columns, with the mirror positions indicated. Successive columns (down, up) are offset in cross-cone by approximately 0.3 pixels, a quirk apparently introduced during launch. In the other dimension (i.e. cone angle), continuous motion of the spacecraft scan-platform displaces the center of each column by approximately one half of a pixel, giving a swath that is 20 pixels high. The nominal effective pixel sizes are 0.5 mrad x 0.5 mrad, but the actual spatial response deviates from an ideal square profile. Laboratory measurements of the spatial responsivity are shown for Det. 6 (1.84 μm) and are representative of the bands used in these observations. In cross-cone the response is triangular, producing overlap between successive mirror positions of a column. The response is more nearly rectangular in the cone angle direction. Some of the response in the tails outside the nominal pixels is due to aberrations in the laboratory collimator, so the actual response is somewhat sharper than indicated.

Fig. 3. Representative spectra of the G fireball. In (a) we show the first NIMS observation obtained 5.17 seconds after the initial PPR detection (the time reference is the same as in Fig. 1), while (b) portrays a spectrum from the middle of the fireball period. The four continuum-wavelengths (1 .84, 2.69, 2.99, and 4.38 μm) were used to obtain the blackbody fits, and absorption by methane has been included. These observations are somewhat higher than neighboring points in time, indicating near ideal instrumental pointing, so these spectra are comparable to the nearly coincident PPR data. The corresponding PPR data (0.945 μm) are shown for comparison. Error limits are shown if larger than the plotting symbol. The derived temperatures are 3251 K and 1834 K respectively; see Fig. 4a for error estimates for these values. The methane absorption curves are derived for absorption above the 75 mbar and 50 mbar levels with an airmass factor of $1 / \cos(\theta_0) = 2.59$. The amount of absorption by shocked Jovian gas compared to that from the external atmosphere is uncertain.

Fig. 4. Derived temperatures and effective diameters for the G fireball. The time reference is the same as that for Fig. 1. Temperatures, shown in (a), include that derived here from PPR and UVS for their initial point at $t = 0$. The effective areas and diameters are given in (b), which indicates a nearly linear change in effective diameter, at least for the first forty-five seconds. The behavior beyond that time is not well established by the measurements. If we assume a constant expansion velocity ($dD_{eff} / dt \approx 3.2$ km see-1) throughout the period, and further assume adiabatic expansion with constant gamma, then a semi-empirical fit to the temperature history shown is found and shown in (a). Other theoretical fits to the temperature and diameter are given later (see Fig. 8).

Fig. 5. Expected values for the adiabatic index y for a hydrogen - helium gas, along with the molecular hydrogen dissociation fraction α. At high temperatures, the energy reservoir available from molecular dissociation gives a large heat capacity and correspondingly a reduced value for the specific heat ratio. Ionization and the inclusion of cometary and other Jovian gases are not included, but would tend to lower the value of y. The dissociation fraction (and therefore the specific heat and α) is pressure dependent; the values used here are representative of debris channel conditions computed with our heuristic model: e.g. pressures of several hundred mbar at 20,000 K, decreasing to a about one mbar at 5000 K.

Fig. 6. Experimental estimate of the adiabatic index gamma from temperature and diameter determinations. If the volume of the emitting surface expands adiabatically and is proportional to D_{eff}^3, the temperature and diameter are related as $TD_{eff}^{3(\gamma-1)} = constant$. Temperature-diameter pairs are shown along with three lines, arbitrarily normalized, whose slope is -3(7 -1) = 1.1, 1.2, and 1.3. The data indicate a value of $\gamma = 1.2 \pm 0.1$. Although it is unlikely that the expanding surface is isothermal, the derived temperatures and gamma seem consistent with expectations (cf. Fig. 5].

Fig. 7. Cartoon of the heuristic fireball model, illustrating the definitions and assumptions. The fragment (radius $_0$)penetrates the atmosphere and creates a high temperature wake or debris channel. Gas within this channel contains an admixture of cometary material, assumed equal by mass to the Jovian gas, and forms a presumed optically thick surface (the debris front). The initial radius of the entry channel is $_0$, but rapidly expands radially to drive an outgoing shock. At the same time, the axial gradient in energy deposition, and therefore pressure, produces an acceleration on the debris material back along the entry path. As the entry channel expands and develops into the fireball, this acceleration and conversion of thermal to kinetic energy produces an axial velocity and mass outflow. The varying energy density due to this flow drives the radial shock in a time-dependent fashion. A narrow region of shear exists between the debris front and the shocked gas just outside. The equations of motion for axial flow and radial shock motion are numerically solved for comparison with the observations.

Fig. 8. Comparison of temperatures (a) and effective diameters (b) with model calculations. The calculations were obtained for various values of the single parameter of the theory - the size of the impactor, assumed to be of unit density. The timing for the data is the same as for Fig. 1; we have placed the time reference t = O for the model computations as that time when the fireball color temperature is 8000°K, the value observed at the onset by the UVS and PPR experiments. The discontinuity at t = 5 sec arises from the fragment penetrating the clouds. The preceding minimum and subsequent rise is likely due to the thermal capacity increasing with depth, producing slower cooling rates. In (a) it can be seen that the computed temperatures in the first 30 sec agree quite well with the data if the G fragment was between 300 and 400 m in diameter. The agreement is unsatisfactory at the latter times, and could be partially due to our approximation for the debris surface temperature, which is expected to be less accurate at longer times. In (b), the effective diameter seems best described by a fragment

diameter of about 200 to 300 m. The decrease in effective diameter at large times is caused by the smaller axial velocities produced in this time period. The emission region shifts down in altitude where debris channel radii are smaller, resulting in a reduced effective luminous area. The same temperature and area estimation procedure was used for both the experimental and theoretical data, so a valid comparison can still be made. Considering the simplicity of the model, the simultaneous agreement of both temperature and diameter estimates of 300 m is pleasing.

Fig. 9. Shape, temperatures, and velocities for the G fireball. This portrays the view presented to *Galileo*. Results are shown for a fragment 300 m in diameter, 26 seconds after the fireball is 8000°K in color temperature (same time reference as in Fig. 8). The spectrum of Fig. 3b is representative of this time. In (a) we illustrate the computed shape of fireball, with the shock and debris boundaries indicated. The asymmetty caused by the vertical atmospheric gradient is apparent. Off-axis motion of the debris channel, as it responds to the asymmetric atmosphere, produces the slight concavity at z ≈ 200 km. The debris front temperature $_d$ is given in (b) along with the 3 μm source function dS/dz. Only altitudes above the ammonia cloud deck were used to derive the temperatures and effective diameters given in Fig. 8 (i.e. only the solid portion of the dS/dz curve). It can be seen that most of the fireball emission occurs above the cloud tops, where the subtended area is largest. The theoretically derived 2, *4* μm color temperature for this time is also indicated in (b). At the right (c), the axial velocity *u* and shock velocities c.(q) are represented. *(q = O* corresponds to radial motion 45 degrees to the zenith).

Fig. 10. Approximate. energy budget for a 300 m diameter fragment. The five principal energy reservoirs are shown as a function of time using the same reference as Fig. 8. The values are approximate due to the finite range of altitudes considered. As the fragment deposits energy, it first appears as thermal energy, with immediate radiative and expansion losses. Radial

expansion results in work being done on the surrounding atmosphere, with the major contribution occurring during the early "bolide" phase. A significant amount of radiative loss occurs during this phase, as indicated by the relatively steep initial slope of the total radiated energy curve. In the present model, much of this early radiative loss occurs below the clouds, but later it occurs in the region above (note that the above-cloud radiation curve parallels the curve of total radiation at later times). The kinetic energy of axial flow increases more slowly and achieves - 15% of the total energy. This energy component is responsible for the splash phase phenomona. Radial flow of the debris channel gas is a minor component of the total. The measured above-cloud integrated luminosity (0.48 ± 0.13 X 1025 erg at t = 60 see, Section IV, Luminosity and Radiated) compares reasonably well (factor of two) with the predicted value for this size fragment, which is shown as the broken curve.

Fig. 11. Time variation of the axial velocity u and mass outflow rate. These quantities are evaluated at 400 km altitude for a 300 m diameter impactor. The time reference is the same as Fig 8. At t ≈ 35 see, both the velocity and the mass flow shows an abrupt increase, with the velocity reaching a peak of $u \approx$ 22 km see^{-1}. The height of the G plume (-3300 km above the 100 mbar level, Hammel et al., 1995) requires a vertical velocity component of -13 km see^{-1} or, with an inclination of 19_0 = 45 degrees, an axial velocity of 18 km see^{-1} to attain that altitude (discounting any addition of the debris front velocity, any viscous interaction, and any elastic collisions of the gas with thermospheric hydrogen). The total mass outflow, integrated between t = O and t = 80 sec is 2.2 x 10^{13} gm.

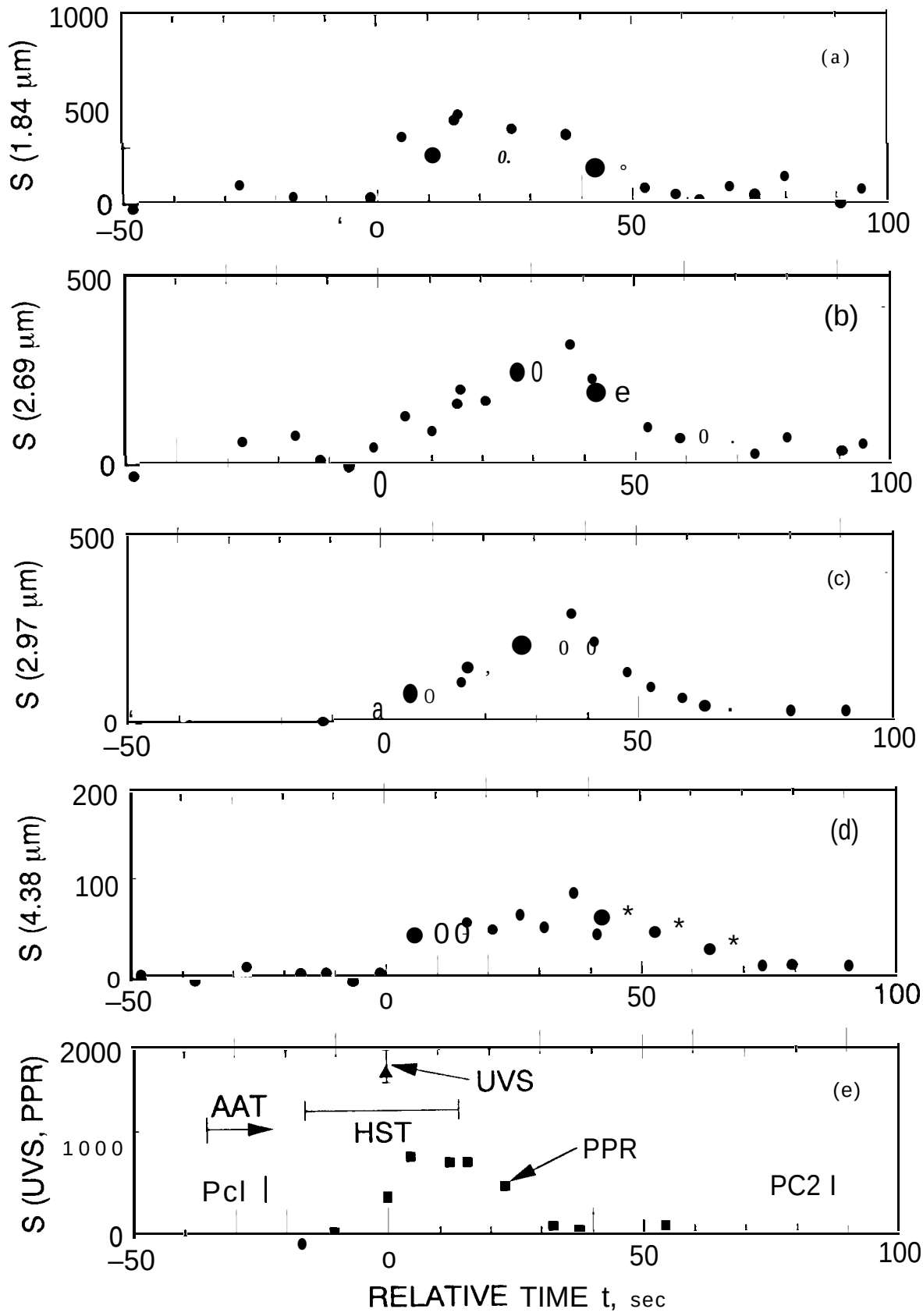
S (1.84 μm)
1000
500
0
(a)
–50
0
50
100
S (2.69 μm)
500
0
(b)
S (2.97 μm)
500
0
(c)
S (4.38 μm)
200
100
0
(d)
S (UVS, PPR)
2000
1000
0
UVS
AAT
HST
PPR
PcI
PC2 I
(e)
RELATIVE TIME t, sec

Fig. 1

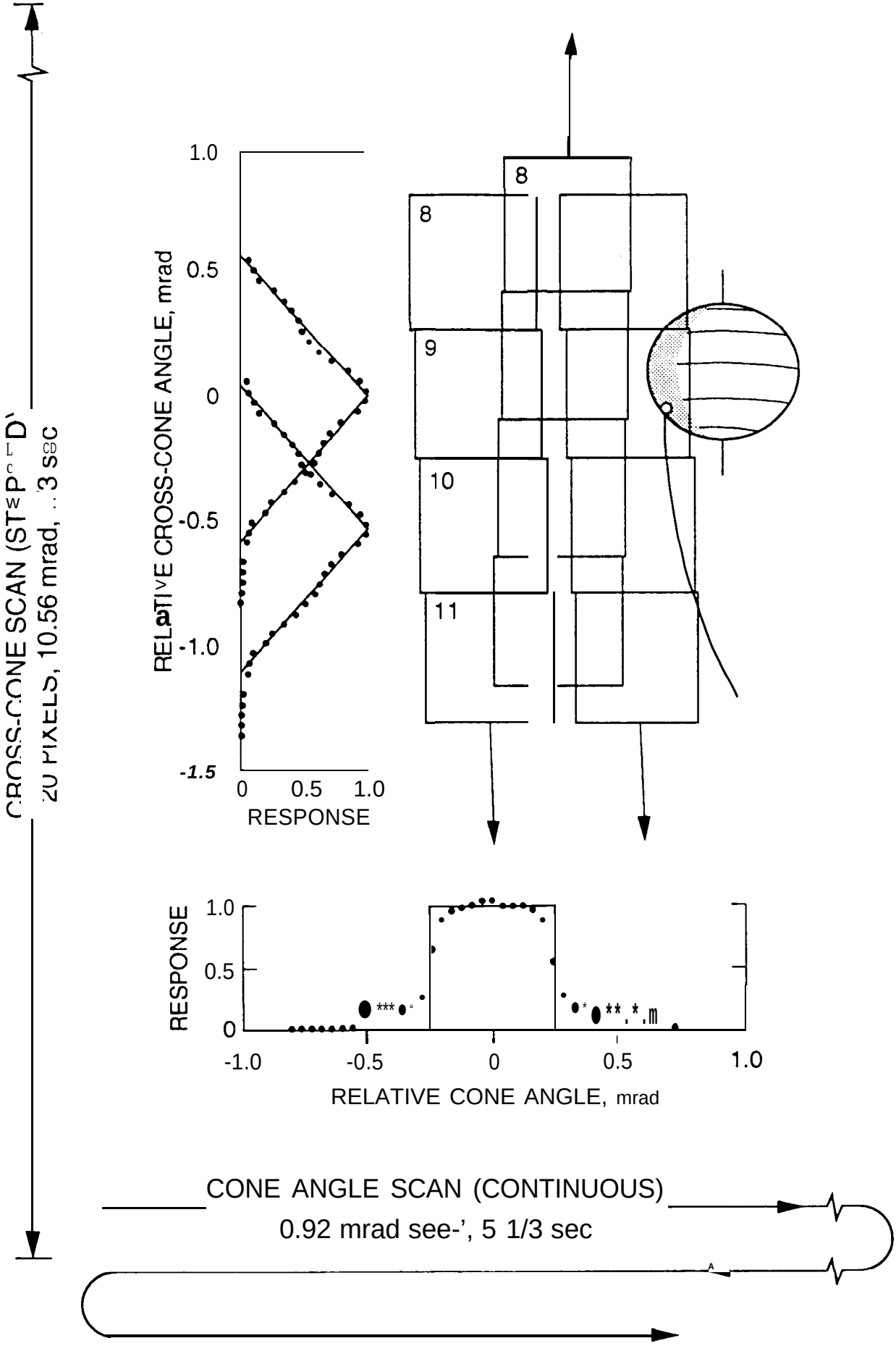
CROSS-CONE SCAN (STEPPED)
20 PIXELS, 10.56 mrad, 3 sec
RELATIVE CROSS-CONE ANGLE, mrad
1.0
0.5
0
-0.5
-1.0
-1.5
0
0.5
1.0
RESPONSE
8
8
9
10
11
RESPONSE
1.0
0.5
0
-1.0
-0.5
0
0.5
1.0
RELATIVE CONE ANGLE, mrad
CONE ANGLE SCAN (CONTINUOUS)
0.92 mrad see-', 5 1/3 sec

Fig. 2

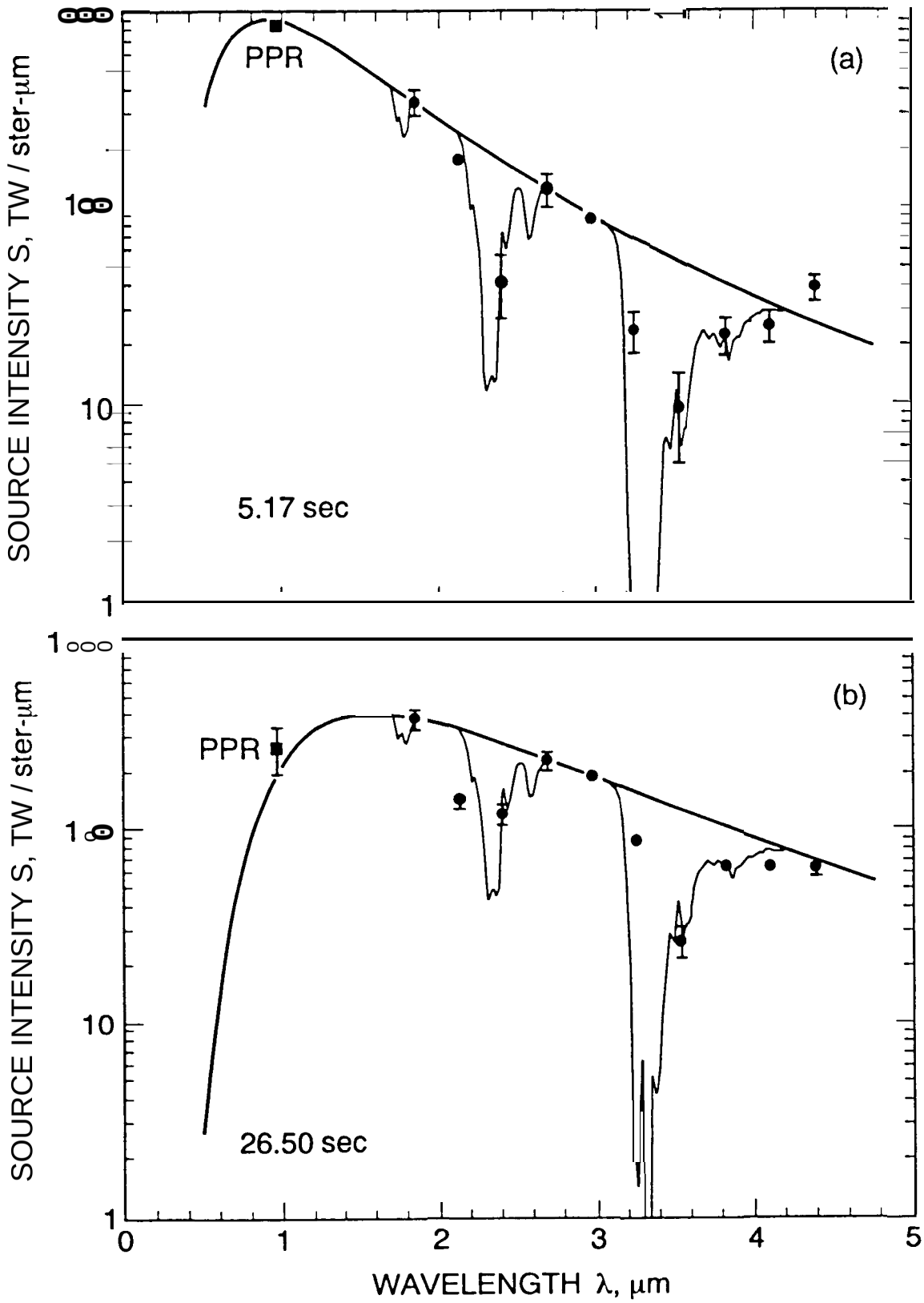
SOURCE INTENSITY S, TW / ster-μm
PPR
(a)
5.17 sec
(b)
26.50 sec
WAVELENGTH λ, μm

Fig. 3

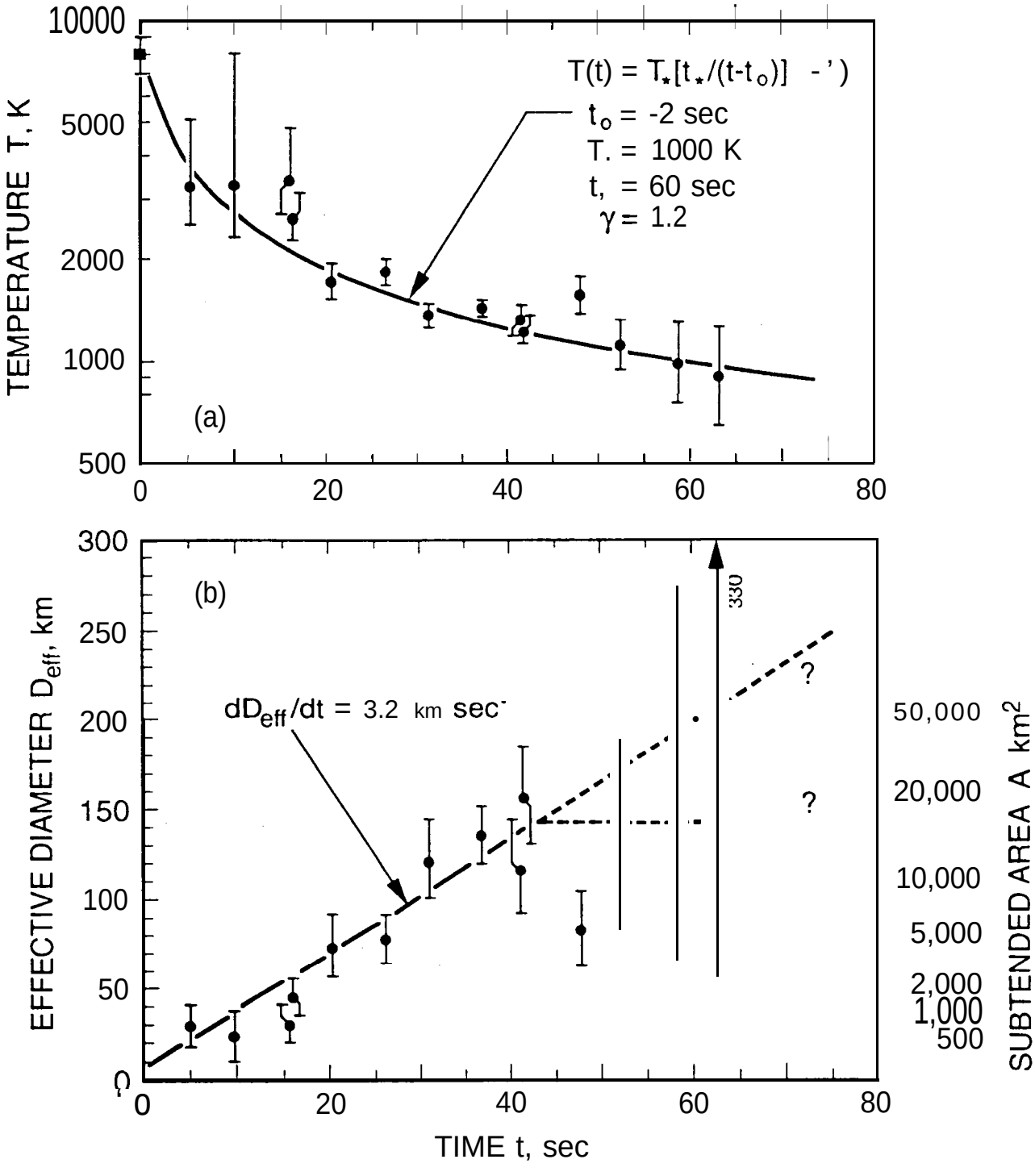
10000
5000
2000
1000
500
TEMPERATURE T, K
T(t) = T*[t*/(t-to)] -')
to = -2 sec
T. = 1000 K
t, = 60 sec
γ = 1.2
(a)
0
20
40
60
80
300
250
200
150
100
50
0
EFFECTIVE DIAMETER Deff, km
(b)
dDeff/dt = 3.2 km sec-
330
?
?
50,000
20,000
10,000
5,000
2,000
1,000
500
SUBTENDED AREA A km2
TIME t, sec

Fig. 4

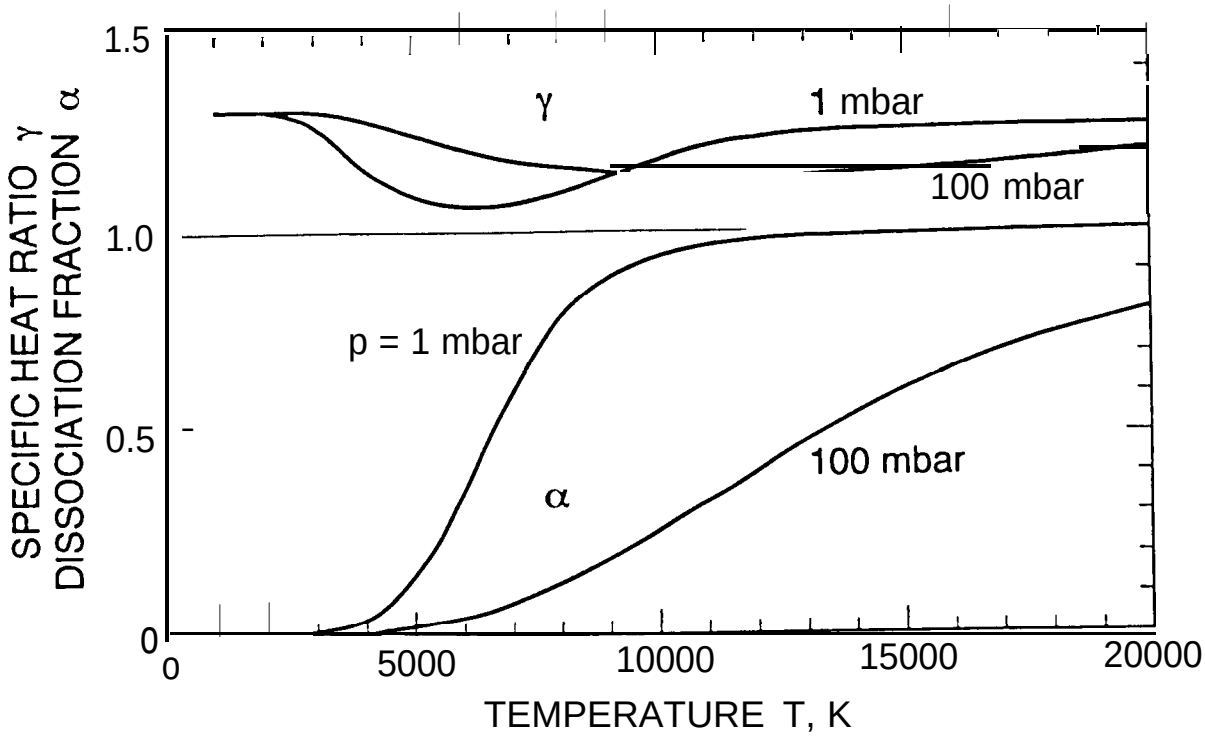
SPECIFIC HEAT RATIO γ
DISSOCIATION FRACTION α
1.5
1.0
0.5
0
γ
1 mbar
100 mbar
p = 1 mbar
α
100 mbar
0
5000
10000
15000
20000
TEMPERATURE T, K

Fig. 5

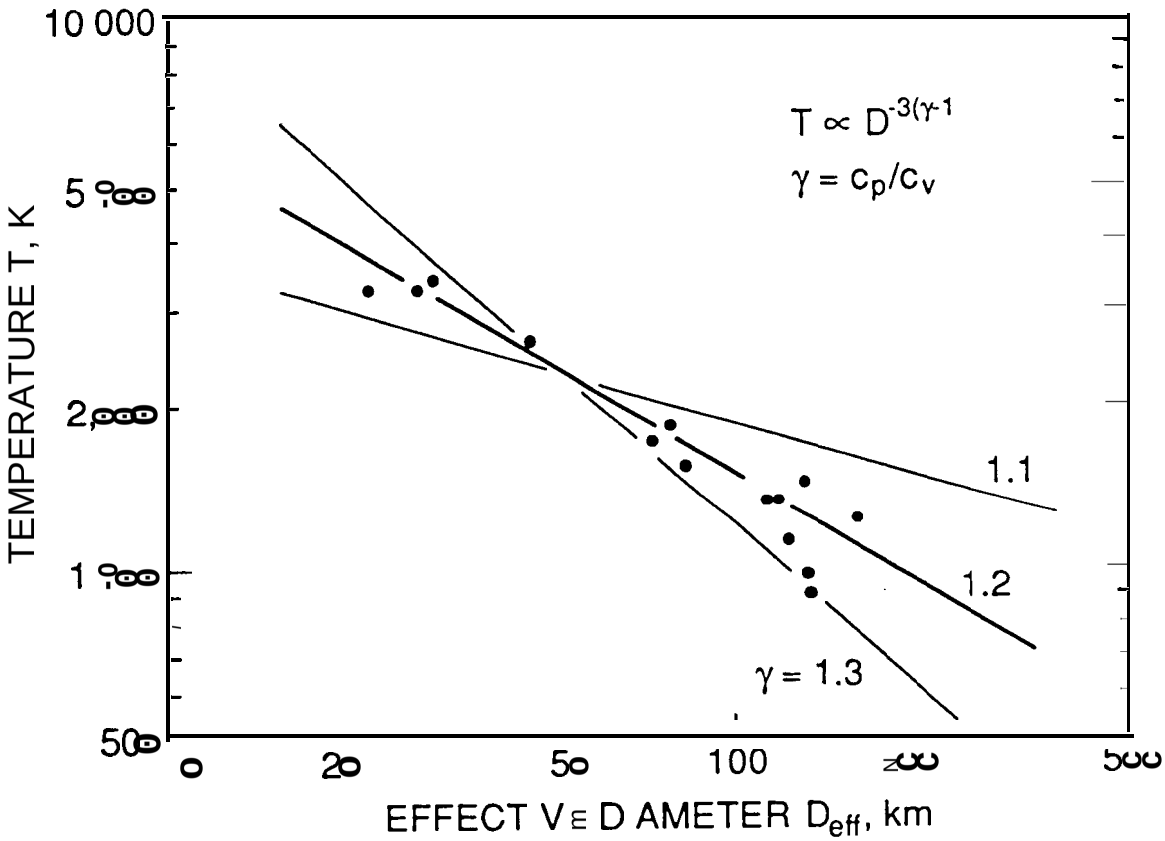
10 000
5 000
2,000
1 000
500
TEMPERATURE T, K
0
20
50
100
200
500
EFFECT VE D AMETER D_{eff}, km
$T \propto D^{-3(\gamma-1)}$
$\gamma = c_p/c_v$
1.1
1.2
$\gamma = 1.3$

Fig. 6

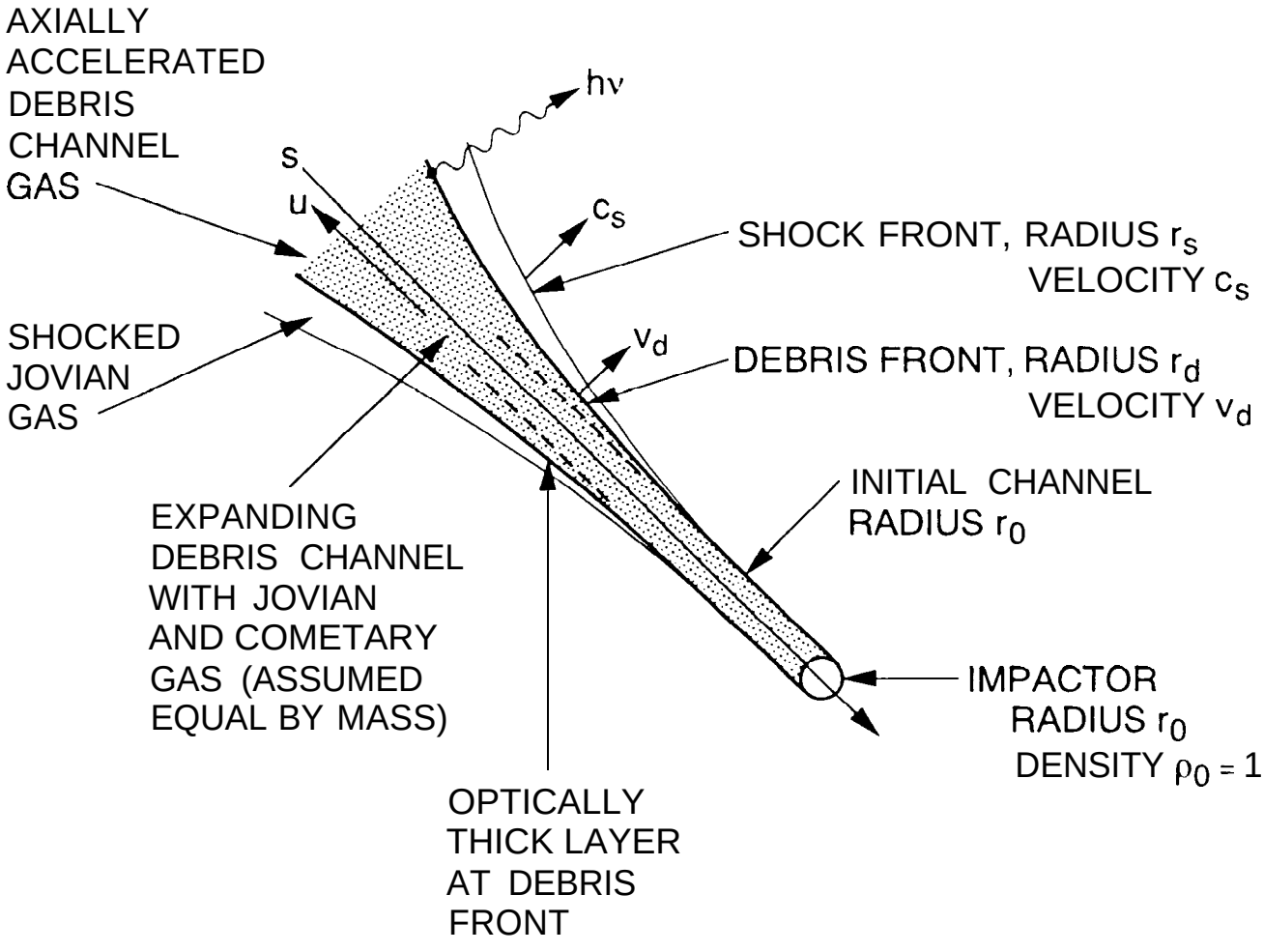
AXIALLY
ACCELERATED
DEBRIS
CHANNEL
GAS
hν
s
u
c_s
SHOCK FRONT, RADIUS r_s
VELOCITY c_s
SHOCKED
JOVIAN
GAS
v_d
DEBRIS FRONT, RADIUS r_d
VELOCITY v_d
INITIAL CHANNEL
RADIUS r_0
EXPANDING
DEBRIS CHANNEL
WITH JOVIAN
AND COMETARY
GAS (ASSUMED
EQUAL BY MASS)
IMPACTOR
RADIUS r_0
DENSITY $\rho_0 = 1$
OPTICALLY
THICK LAYER
AT DEBRIS
FRONT

Fig. 7

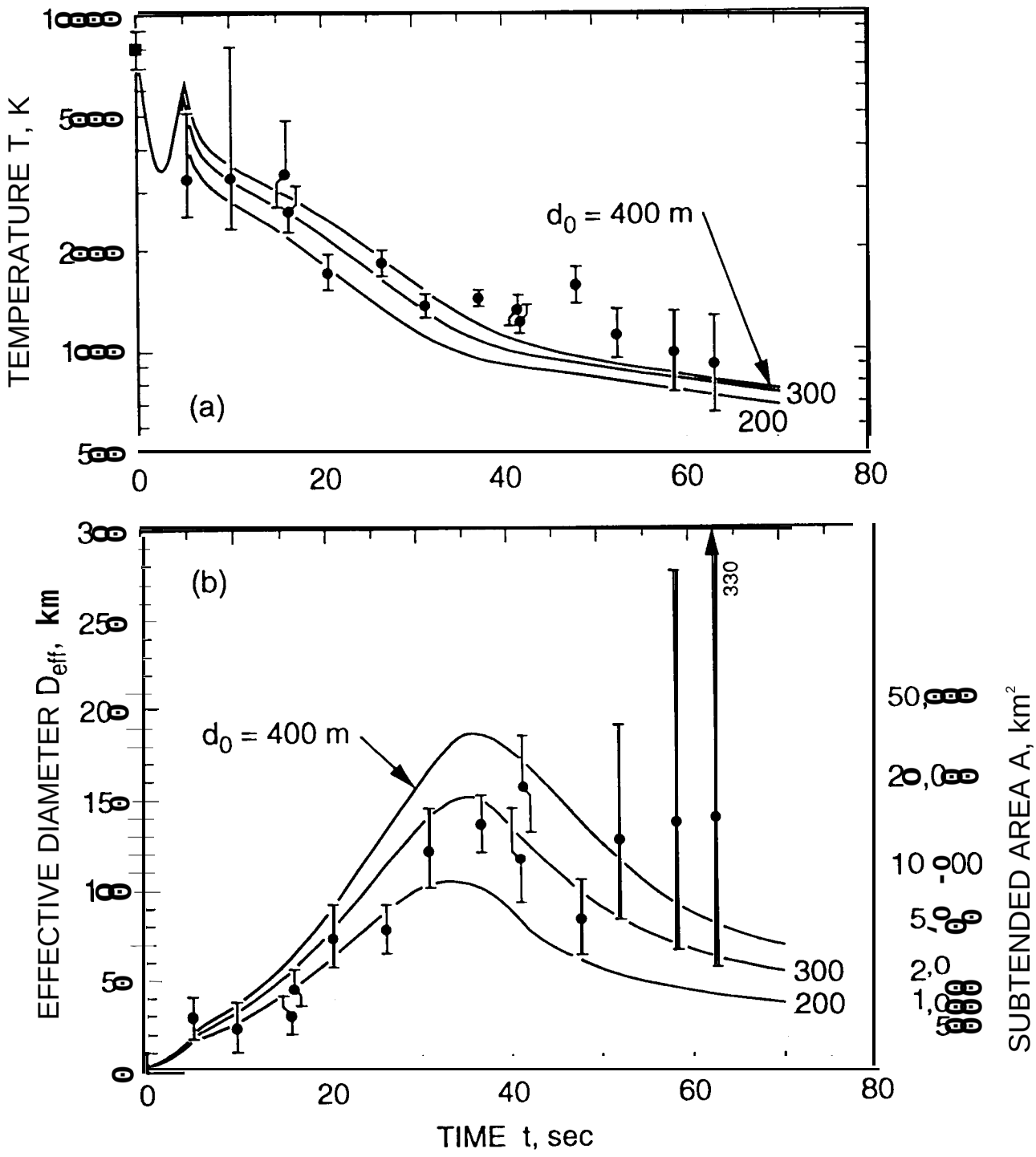
TEMPERATURE T, K
10000
5000
2000
1000
500
(a)
d_0 = 400 m
300
200
0
20
40
60
80
(b)
EFFECTIVE DIAMETER D_{eff}, km
300
250
200
150
100
50
0
330
d_0 = 400 m
300
200
50,000
20,000
10,000
5,000
2,000
1,000
500
SUBTENDED AREA A, km^2
TIME t, sec

Fig. 8

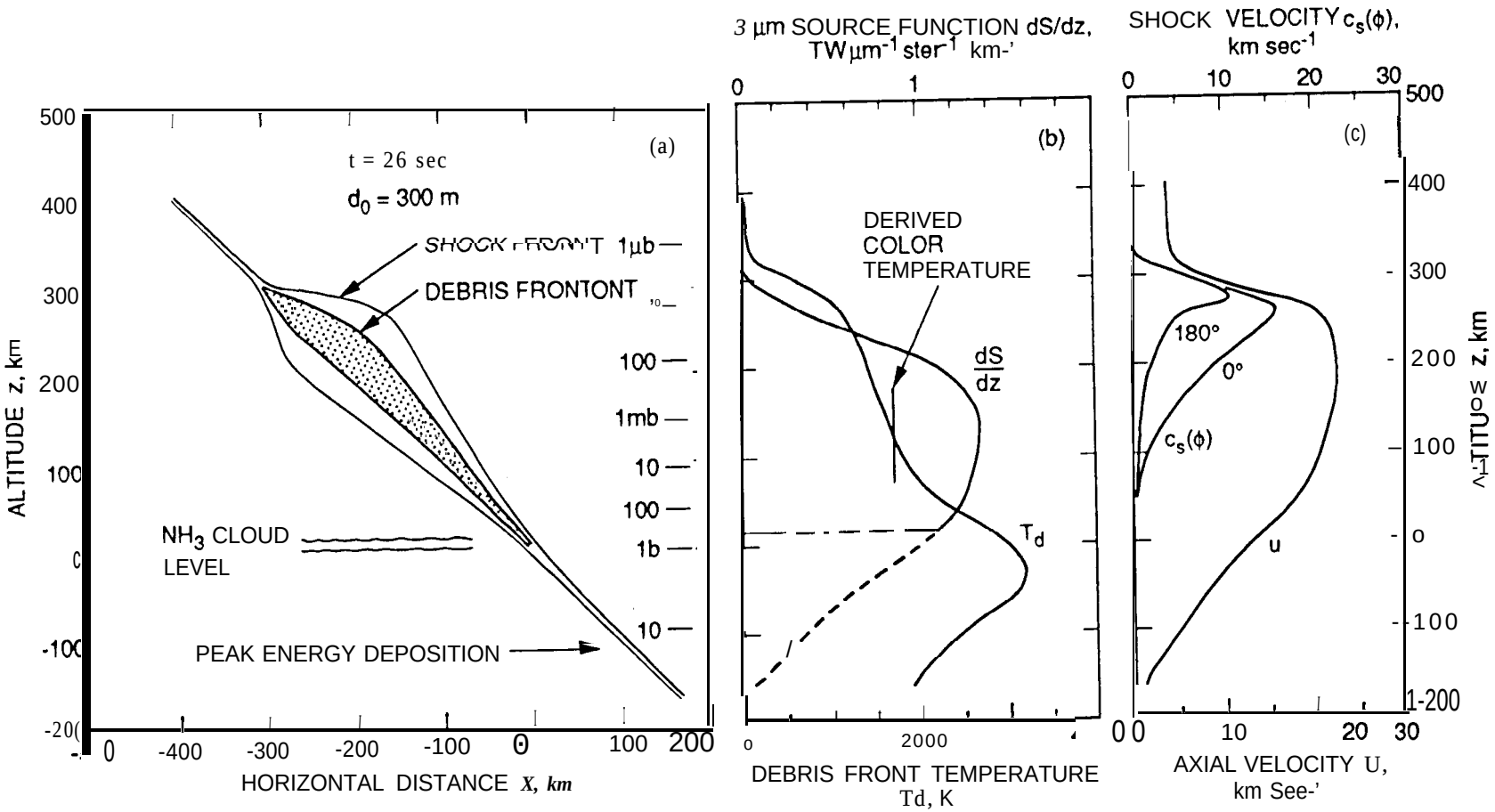
(a)
t = 26 sec
d_0 = 300 m
SHOCK FRONT 1μb
DEBRIS FRONTONT
100
1mb
10
100
1b
10
NH_3 CLOUD LEVEL
PEAK ENERGY DEPOSITION
ALTITUDE z, km
HORIZONTAL DISTANCE X, km
3 μm SOURCE FUNCTION dS/dz, TW μm^{-1} ster^{-1} km^{-1}
(b)
DERIVED COLOR TEMPERATURE
dS/dz
T_d
DEBRIS FRONT TEMPERATURE Td, K
SHOCK VELOCITY $c_s(\phi)$, km sec^{-1}
(c)
180°
0°
$c_s(\phi)$
u
AXIAL VELOCITY U, km See^{-1}
ALTITUDE z, km

Fig. 9

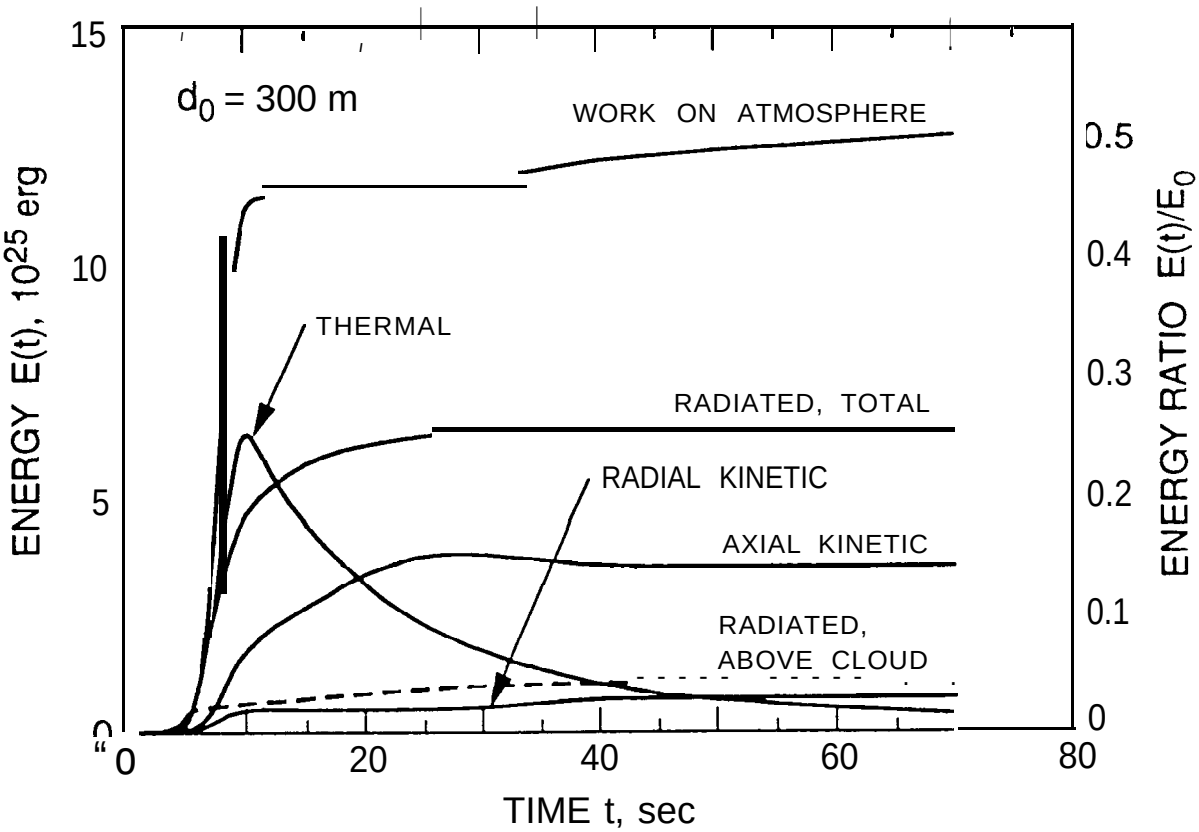
15
10
5
0
d_0 = 300 m
WORK ON ATMOSPHERE
THERMAL
RADIATED, TOTAL
RADIAL KINETIC
AXIAL KINETIC
RADIATED,
ABOVE CLOUD
ENERGY E(t), 10^{25} erg
0.5
0.4
0.3
0.2
0.1
0
ENERGY RATIO $E(t)/E_0$
0
20
40
60
80
TIME t, sec

Fig. 10

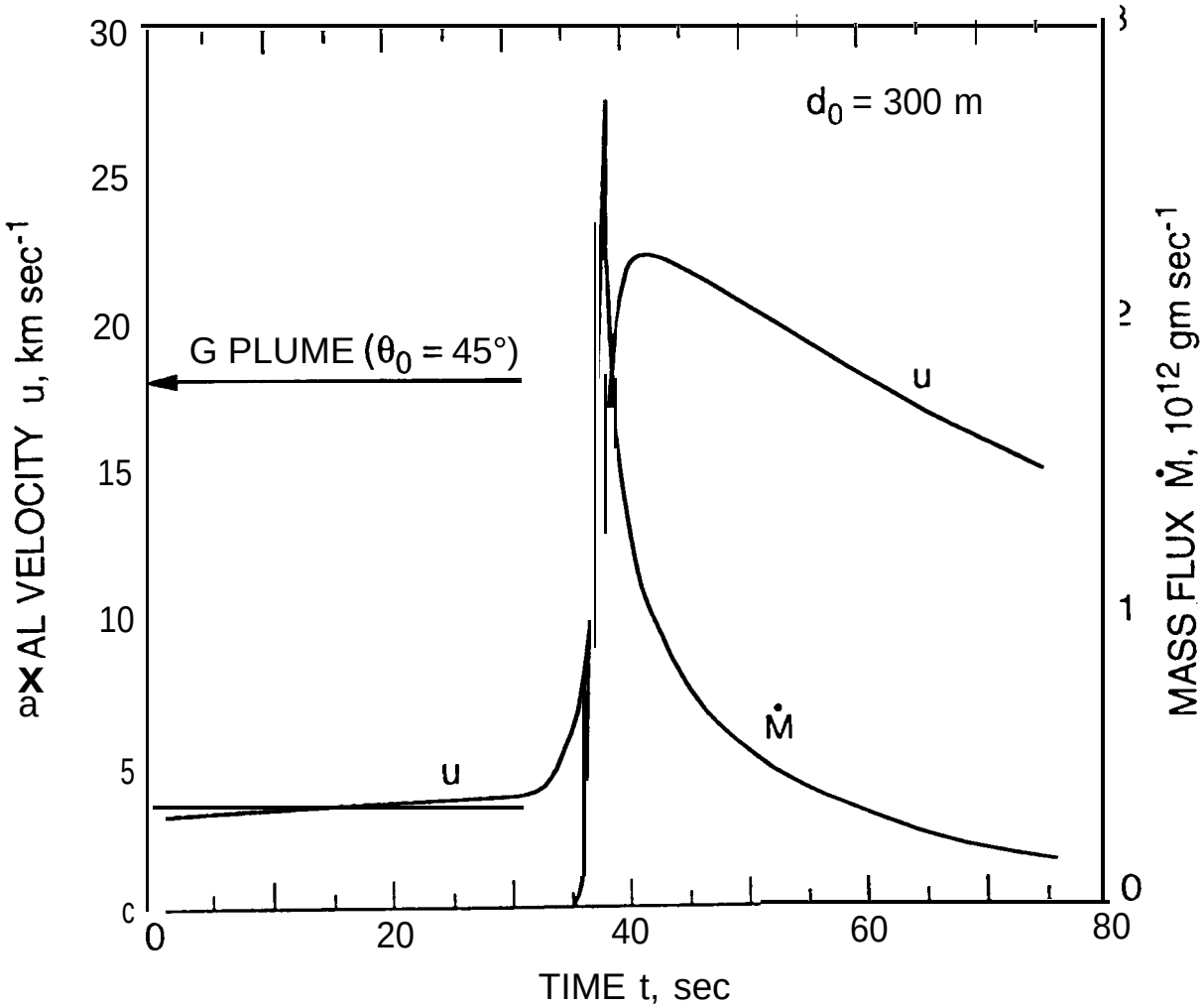
30
25
20
15
10
5
0
0
20
40
60
80
TIME t, sec
d_0 = 300 m
G PLUME (θ_0 = 45°)
u
u
$\dot{M}$
MASS FLUX $\dot{M}$, 10^{12} gm sec^{-1}
1
0

Fig. 11